
Article:
Nation, DD, Heggs, PJ orcid.org/0000-0003-3209-6521 and Dixon-Hardy, DW (2017) Modelling and simulation of a novel Electrical Energy Storage (EES) Receiver for Solar Parabolic Trough Collector (PTC) power plants. Applied Energy, 195. pp. 950-973. ISSN 0306-2619

https://doi.org/10.1016/j.apenergy.2017.03.084

Modelling and Simulation of a Novel Electrical Energy Storage (EES) Receiver for Solar Parabolic Trough Collector (PTC) Power Plants

Deju D. Nation[1]*, Peter J. Heggs[2], Darron W. Dixon-Hardy[2]

[1]*Department of Mathematics and Engineering, Northern Caribbean University Jamaica W.I.*
[2]*School of Chemical and Process Engineering, University of Leeds, United Kingdom*

Abstract

In this paper, the mathematical modelling of a novel Electrical Energy Storage (EES) Receiver for Solar Parabolic Trough Collector (PTC) is presented. The EES receiver is essentially a Heat Collecting Element (HCE) with built in storage in the form of thermal batteries such as the Sodium Sulphur (NaS). The conceptual design and mathematical models describing the operation of the receiver are presented along with important results of model validation. When held under adiabatic conditions (a primary indicator of model validity), results were highly consistent with established National Renewable Energy Laboratory(NREL), USA models and with experimental data for existing SCHOTT PTR-70 and Solel UVAC3 receiver tubes currently being used in existing PTC power plants.

Keywords: Energy Storage, Parabolic Trough Collector, PTC, Power Plants, Heat Collecting Element, HCE, Thermal Battery, Sodium Sulphur, Utility Grid, NaS Cell

Nomenclature

Parameter	Description	Unit	Parameter	Description	Unit
A_{col}	Collector mirror area	(m^2)	$\alpha_{conv,gt}$	Convective heat transfer coefficient from glass tube to ambient	($Wm^{-2}K^{-1}$)
ε_{at}	Emissivity of absorber tube	None	$\alpha_{conv,at}$	Convective heat transfer coefficient from absorber tube to glass tube	($Wm^{-2}K^{-1}$)
ε_{gt}	Emissivity of glass tube	None	$D_{at,o}$	Outer diameter of absorber tube	(m)
τ_{gt}	Transmittance of glass tube	None	$D_{at,i}$	Inner diameter of absorber tube	(m)
α_{at}	Absorptance of absorber tube	None	$D_{gt,o}$	Outer diameter of glass tube	(m)
α_{gt}	Absorptance of glass tube	None	$D_{gt,i}$	Inner diameter of glass tube	(m)

Parameter	Description	Unit	Parameter	Description	Unit
$\mathfrak{I}_{gt,o}$	Shape Factor of glass tube outer surface	None	$D_{bt,o}$	Outer diameter of battery tube	**(m)**
$\mathfrak{I}_{a,o-gt,i}$	Shape Factor between absorber and glass tubes	None	$D_{bt,i}$	Inner diameter of battery tube	**(m)**
$K_{\tau\alpha\gamma}$	Incidence angle modifier	None	D_{NaS}	Diameter of the NaS cell's inner sodium electrode	**(m)**
σ	Boltzman's Constant	($Wm^{-2}K^{-4}$)	$T_{gt,i}$	Temperature of glass tube inner wall	**(K)**
k_{ab}	Thermal conductivity of material between "a" and "b".	($Wm^{-1}K^{-1}$)	$T_{gt,o}$	Temperature of glass tube outer wall	**(K)**
γ	Mirror Shape Factor	None	T_{htf}	Bulk heat transfer fluid temperature	**(K)**
ρ	Mirror reflectivity	None	T_{sky}	Sky Temperature	**(K)**
$h_{ann,o}$	Outer annular heat transfer coefficient	($Wm^{-2}K^{-1}$)	T_{amb}	Ambient Temperature	**(K)**
$h_{ann,i}$	Inner annular heat transfer coefficient	($Wm^{-2}K^{-1}$)	$\overline{T}_{NaS}$	Average temperature of the NaS cell in lumped model	**(K)**
$T_{at,o}$	Temperature of absorber tube outer wall	(K)	$T_{at,i}$	Temperature of absorber tube inner wall	(K)
$T_{bt,o}$	Temperature of battery tube outer wall	(K)	$T_{bt,i}$	Temperature of battery tube inner wall	(K)
$T_{bt,o}$	Temperature of battery tube outer wall	(K)	$T_{bt,i}$	Temperature of battery tube inner wall	(K)
E_{cell}	NaS cell voltage w.r.t cell discharge state	(V)	CR	Solar Flux Concentration Ratio	**None**
I_{cell}	NaS cell current (charging –ve, discharging +ve)	(A)	R_{NaS}	Internal electrical resistance of NaS cell	**(Ω)**
Nu	Nusselt Number	None	**Pr**	Prandtl Number	None
Gr	Grashof Number	None	**Re**	Reynolds Number	None
Ra	Rayleigh Number	None	**Bi**	Biot Number	None

Table 1: Definition of Heat Fluxes for EES Receiver

Heat Flux (W/m)*	Heat Transfer Method	Heat Transfer Direction	
		From	To
$\dot{q}'_{htf-NaS}$	Conduction	heat transfer fluid	NaS cell
$\dot{q}'_{cond,bt}$	Conduction	battery tube outer surface	battery tube inner surface
$\dot{q}'_{htf-bt,o}$	Convection	heat transfer fluid	battery tube outer surface
$\dot{q}'_{at-htf}$	Convection	absorber tube inner surface	heat transfer fluid
$\dot{q}'_{cond,at}$	Conduction	absorber tube outer surface	absorber tube inner surface
$\dot{q}'_{Lrad,at-gt}$	Radiation	absorber tube outer surface	glass tube inner surface
$\dot{q}'_{Lcond,gt}$	Conduction	glass tube inner surface	glass tube outer surface
$\dot{q}'_{Lconv,gt-amb}$	Convection	glass tube outer surface	Ambient
$\dot{q}'_{Lrad,gt-sky}$	Radiation	glass tube outer surface	Sky
$\dot{q}'_{sol.abs,at}$	Radiation	Sun	Abs. tube outer surface
$\dot{q}'_{sol.abs,gt}$	Radiation	Sun	glass tube outer surface
$\dot{q}'_{Lgt,tot}$	convection, radiation	Sun	Ambient
$\dot{q}'_{bt,i-NaS}$	Conduction	battery tube inner surface	NaS cell

***** per unit length of the EES receiver

1. Introduction

Solar parabolic trough collector (PTC) power plants have been at the core of modern utility scale solar power generation for over three decades [1]. This is largely due to the fact that they produce large amounts of *"green"* dispatchable electric power on a Mega Watt (MW) scale, through thermo-electrical conversion of concentrated solar radiation using precisely engineered solar collector/receiver assemblies (Figure 1)[2]. When integrated with storage, they can provide a great potential for the integration of other Variable Renewable Energy (VRE) technologies and a host of other ancillary and power quality support applications [3],[4].

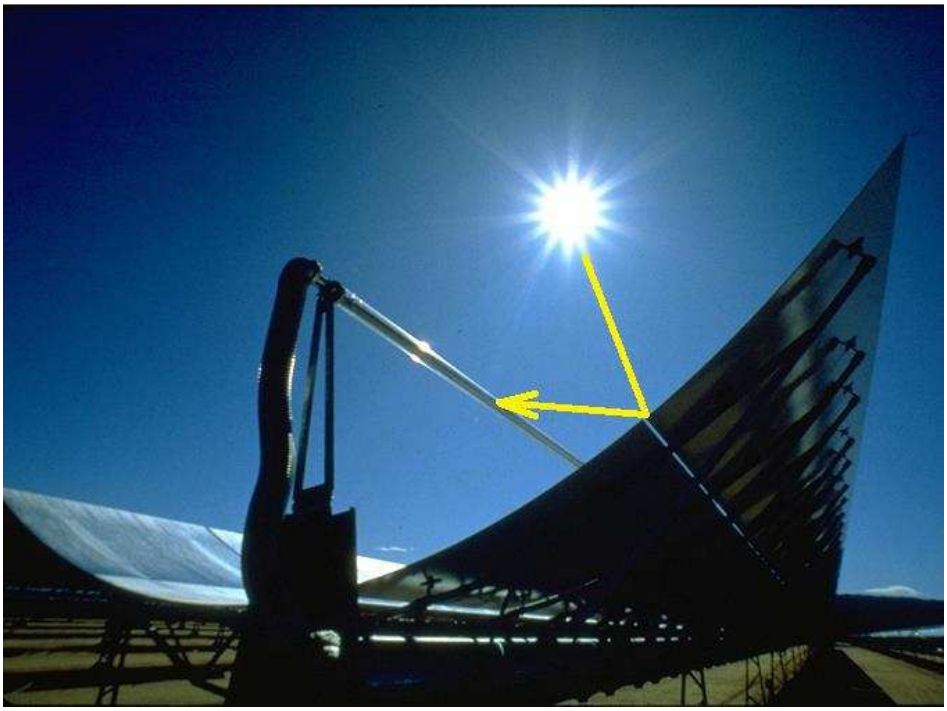

Figure 1: Parabolic trough collector and receiver tube (Source: NREL)

However, a survey of widely available literature on renewables reveal that in recent years, commercial and utility scale PTC technology has been adversely affected by falling prices in photovoltaic technology, its main competitor [5]. If PTC technology is to become a more attractive to investors in a market swamped with low cost photovoltaics, news ways must be found to leverage or enhance a key advantage of this technology, *"energy storage capability".* While examining storage options, it was discovered that high energy density *"Sodium Sulphur (NaS)"* batteries were being deployed for electrical energy storage applications in wind and Photovoltaic (PV) plants worldwide [6].

It was also realized that these battery systems were widely used for grid support applications in Japan, providing power outputs in the MW range for over 6-8 hour durations [7]. It is this 6-8 hour power supply duration that initially prompted interest in the energy storage

capabilities of these battery systems, as it is identical to the average power supply duration of a PTC plant thermal storage system. Also the fact that NaS batteries are thermal batteries and must be heated up to operational temperature before use, led to the realization that the NaS battery and a standard PTC power plant both operate within a coincidental temperature range of 300 – 400°C [8],[9].

This immediately suggested that it would be possible to heat the NaS batteries using the HTF from the solar field, a completely different method to the standard approach of heating these batteries in a sand filled module equipped with an electrical heater and a temperature control system [10]. It also became apparent that the tubular nature of most commercial NaS cells would allow them to be easily placed inside a standard PTC receiver tube for heating [11]. All that would be required was a special modification of the receiver tube internals to allow for heat transfer fluid (HTF) flow between the main receiver tube and the internal batteries (annular flow) rather than traditional plugged flow [12].

This sequence of initial thought processes led to the conceptualization, design, modelling and analysis of the Electrical Energy Storage (EES) Receiver for Solar Parabolic Trough Collectors (PTC's), described in Section 3. However, it is great important to contextualize this work in relation to recent advances in the Energy Storage and NaS Battery technologies. This is covered in the survey of recent, relevant literature which follows next.

2. Literature Review – A Survey of Recent Progress in Energy Storage Technologies for Solar and General Renewable Energy Applications

The creation of an innovative energy storage solution is a central focus of this paper. Consequently, the existing and emerging energy storage technologies in their various modes of development and deployment serve as the background for the contextualizing this work.

2.1. General Energy Storage Applications

Energy storage technologies have seen significant and increasing deployment in renewable energy systems in recent years. This is particularly due to their ability to increase the value of the energy produced from variable renewable energy (VRE) sources by reducing energy curtailment and significant increasing energy dispatchability [13]. Further, the scope of energy storage technologies under current research and development is extremely broad. A survey of the most recent review comprehensive articles [13–26] on this topic reveals that current energy storage systems for domestic, commercial and utility markets cover a very wide a broad scope of technologies. These include, but are not limited to the following:

- Pumped-Hydro Energy Storage (PHES)
- Underground Thermal Energy Storage (UTES)
- Compressed Air Energy Storage (CAES)

- Liquid Air Energy Storage (LAES)
- Molten Salt/Synthetic Oil Thermal Energy Storage
- Electrical/Electrochemical Battery Storage
- Supercapacitor Short Term Energy Storage
- Flow Battery Energy Storage
- Thermochemical/Thermo-electro-chemical Storage
- Chemical-Hydrogen Storage
- Flywheel and Mechanical Spring Storage
- Superconducting Magnetic Energy Storage (SMES)
- Solid Media/Phase Change Energy Storage
- Hot/Cold Water Energy Storage

An evaluation of the above listing reveals that these systems store available energy either in electrical, chemical, gravitational potential, elastic potential or thermal energy forms and cover a capacity ranging from Watt-hours (Wh's) to Giga-Watt-hours (GWh's) [23]. They also cover a time span ranging from short-term usage (e.g. electric grid frequency control, ramping and spinning reserves), to medium term grid supply/demand balancing, up to long-term storage options (such as seasonal energy storage, or as substitutions for grid extensions/reinforcements)[13].

Increasingly, many of the above-mentioned storage technologies are now being deployed as Hybrid Energy Storage Systems (HESS). As stated by Bocklisch and Chong *et al*., these systems provide a beneficial coupling of two or more storage systems that increases the durability, practicality and cost effectiveness of a passive, semi-active or active storage solution[27,28]. Recent comprehensive reviews of HESS technologies by Hematti *et al.* and Zimmermann *et al.* [29,30] discuss standard HESS applications, coupling architectures, energy management mechanisms and approaches for power flow decomposition using peak shaving and double low-pass filtering approaches.

With respect to low and short term power scales, flywheels, mechanical springs, superconducting magnets and supercapacitors are the technologies of choice for absorbing and supplementing intermittent mismatches in energy supply and demand for electric grids. In many instances, they also aid with power quality support in the form of voltage/frequency control. Recent comprehensive reviews of these Energy Storage Systems (FESS) as conducted by Arani *et al.*, Buckles *et al.*, Pena-Alzola *et al.*, Raman *et al.* and Mousavi *et al.* [31–37] suggest among other things that these technologies will all play an increasing role in supporting renewables energy penetration of utility grids; extending the economies scale seen in large scale storage applications such as Pumped Hydro Energy Storage (PHES) technology to lower power "building level" scales where this is absent [38] and providing "smoothing power support" in microgrids.

For higher and longer power scale applications, especially in support of baseload power generation, electro-mechanical/ storage technologies such as Pumped-Hydro Energy Storage (PHES), Compressed Air Energy Storage (CAES), Liquid Air Energy Storage (LAES) and electro-chemical Flow Battery Energy Storage (FBES) are in current use. Of this group PHES is the most dominant and mature technology, accounting for 99% of current global grid energy storage capacity and is readily able to provide flexible ramping and power quality services [23,39]. CAES and LAES are emerging storage options on the medium to large power scale. However, as stated by Budt *et al*., these technologies must overcome significant challenges such as their various degrees of ramping inflexibility; site dependent and high cost air reservoirs and in many cases, the conversion inefficiencies associated with the use of separate compressors and turbines within the energy conversion cycle [40].

With respect to Flow Battery Energy Storage (FBES), Alotto *et al.* and Weber *et al.* in a recent reviews highlighted the high potential of this storage technology, citing positives such as high cycle efficiencies, power/energy independent system sizing, room temperature operation, and very long working cycle life [41,42]. However, one significant hurdle to expansive commercial deployment of these systems (eg. zinc-bromine, vanadium and iron–vanadium and other common redox couples) is their significant capital cost [43,44].

2.2. Solar Energy Storage Applications

Solar energy systems are among the most promising and increasingly deployed renewable energy technologies. These systems are divided largely into two major categories; Solar Photovoltaics (PV) and Solar thermal technologies. Each of these two categories may be implemented at the systems level as concentrating solar power (CSP) systems or non-concentrating systems. Owing to the intermittent nature of solar energy sources, storage systems are especially critical for grid integration and increased renewables penetration [25]. However, none of the previously described energy storage solutions are utilized or deployed with existing utility scale solar energy systems.

Historically, storage solutions for utility scale solar energy systems have been largely electrical/electro-chemical for Photovoltaic Systems and Thermal/Thermo-chemical/Thermo-electrical for Solar Thermal Systems. Solar photovoltaic systems have been traditionally augmented with electrical energy storage on the residential/commercial side mainly in the form of deep cycle lead acid or lithium-ion batteries [45]. On a utility scale, both solar photovoltaic and wind energy systems have been augmented with electrical energy storage in the form of Sodium-Sulfur and Redox Flow batteries in a few reported pilot projects [8,46–50].

This work however concerns Solar Parabolic Trough Collector (PTC) systems, a thermally categorized utility scale concentrating solar power (CSP) technology that has traditionally utilized low cost sensible heat storage in insulated tanks with eutectic mixtures of KNO_3,

$NaNO_3$ molten salts[51]. The traditional set-up is that of a two-tank system (a hot and cold tank) operated in conjunction with a heat exchanger and the solar collector field [52]. This is the industry standard used in all operating utility scale CSP power plants to date. Through successful research has been conducted on solid media storage mechanisms such as high temperature concretes, phase change encapsulated solids, cast iron, cast steel, silica and magnesia fire bricks [53], no utility scale storage system based on these technologies currently exists.

One promising tank based storage system is the "thermocline", in which both hot and cold fluid are contained in a single tank. The term "thermocline" refers to the the sharp temperature gradient that exists between the two fluid regions and which serves as a boundary of fluid separation. The separation between "hot" and "cold" fluid regions is maintained by the combined effect of buoyancy induced stratification within the storage and/or by a movable baffle that floats up or down within the tank. Conceptually, this storage system could provide a lower cost storage solution, but there have been challenges with maintaining fluid stratification and preventing heat transfer between the two fluid regions

One of the earliest deployments of this storage system was the Solar One Thermocline Tank which operated from 1982 to 1986 using Caloria HT-43 mineral oil as a heat transfer fluid and a rock/sand combination as the porus filler material [54]. Over a decade ago Pacheo *et al*. and Brosseau *et al.* of Sandia National Laboratories pioneered experimental work on 2.3 MWh_{th} pilot thermocline tank [55,56]. Research in recent years has focused mainly on four key areas (a) Optimization of tank design (b) Filler material selection and analysis (c) General thermocline system modelling and (d) Investigating thermal ratcheting and viscous channelling problems [55–64].

Thermo-chemical energy storage systems have also been researched and developed for use with solar thermal systems. These range from systems that produce usable fuels such as hydrogen and syngas by feedstock dissociation, using concentrated solar radiation [65–72] to multilevel sorption based "thermal battery" cascaded storage systems [73–81]. Thermochemical energy storage systems are therefore promising either for producing "green substitute fuels" or for serving as thermal battery systems, especially useful when scavenging waste heat from industrial processes. However, these technologies still have not realized mainstream competitiveness with the traditional two-tank thermal storage systems used in utility scale solar projects and are still under intense research and development.

This concludes a succinct review of the relevant literature in recent years on energy storage systems. The concept proposed in this work, that of hybridizing Sodium-Sulphur Battery and Parabolic Trough Collector technologies in a hybridized EES Receiver, is an expansion of an original concept proposed by the authors of this work in an earlier publication [82]. This survey of published literature clearly establishes the EES Receiver storage concept as both a novel contribution and an enhancement to the body of published literature on conceptual solar energy storage systems.

The section which follows next begins with a description of the conceptual EES receiver, the principal subject of this work.

3. Description of the EES Receiver

The EES receiver can be described as a hybrid solar heat collecting element (HCE) for parabolic trough collectors with built in electrical storage. The objective behind the design of the EES receiver was to create a solar receiver for that could help to solve the challenge of energy storage by incorporating *"built in energy storage"*.

Unlike the traditional receiver (Figure 2a) used in a PTC power plant, the conceptual EES receiver (Figure 2b) would provide the functions of a traditional PTC receiver along with the added benefit of electrical energy storage in the form of sodium sulphur batteries. Although technically speaking, *"a battery is an electrical connection of two or more cells"*, throughout this paper the terms *"NaS battery"* and *"NaS cell"* are used interchangeably, as referring to *"a single NaS energy storage element"*.

The longitudinal section through the EES receiver (Figure 2) highlights the fundamental difference of the EES receiver with respect to a standard PTC receiver. This difference lies in its internal construction.

Like a traditional receiver (e.g Schott PTR-70), the EES receiver consists of a selectively coated steel absorber tube enclosed within an evacuated borosilicate glass cover, with glass and metal tube ends joined together through use of thermally expandable steel bellows and glass-metal seals [83]. The glass cover itself has high transmittivity to solar flux ($\tau_g > 0.97$) and has an anti-reflective coating to reduce reflective losses.

Vacuum enclosure of the absorber tube protects the selective coating from degradation and virtually eliminates convective heat loss. Special chemical getters (molecule sponges) placed within the evacuated space, absorb gas molecules left after sealing and indicate via colour change, whether the tube's vacuum has been lost. All of the above is typical of a commercial PTC receiver [84,85]. In addition to all the afore mentioned components, the EES receiver contains an internal "battery tube" (Figure 3) containing high energy density NaS cells or equivalent thermal batteries. The heat transfer fluid (HTF) therefore flows in the *"concentric annular space"* between the absorber and battery tubes.

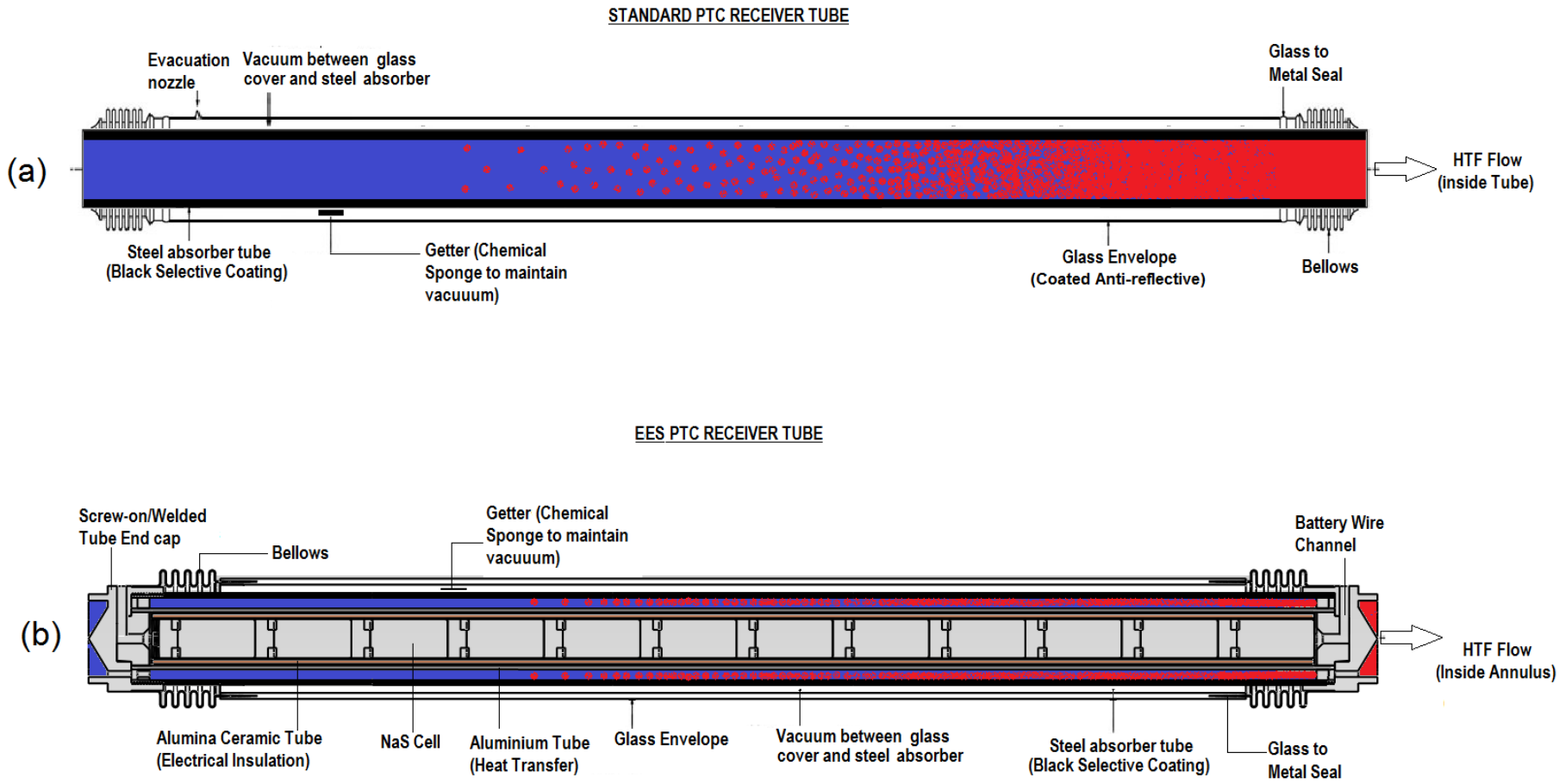

Figure 2: Schematic showing (a) Section through Standard Receiver Tube and (b) Conceptual EES Receiver Tube

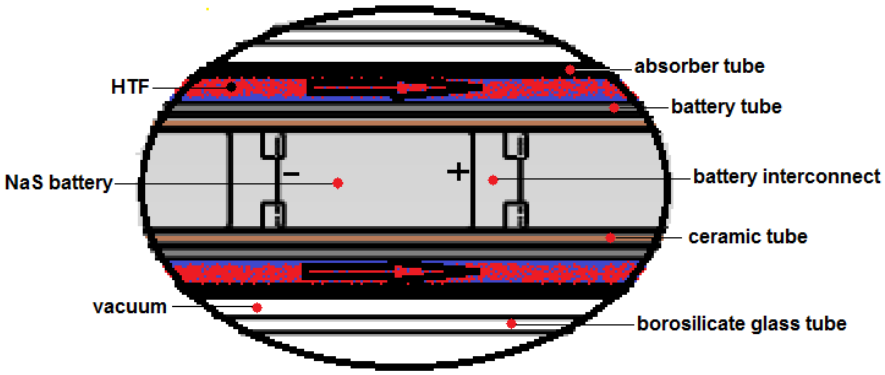

Figure 3: Schematic showing internal assembly of tubes within the EES Receiver

Heat is transferred through forced convection from the HTF to the battery tube wall, which should be made of a highly thermally conductive material such as aluminium, capable of the process duty (temperature and pressure). For higher temperature systems (T > 500°C), a steel battery tube would be required. Inside the battery tube, is a special ceramic tube (Figure 3) which houses the NaS batteries. The fundamental purpose of this tube is to electrically insulate NaS batteries from each other and also from the rest of the receiver, thereby preventing short circuiting. Therefore, this tube should be electrically non-conductive.

However, since heat must be transferred from the battery tube to the NaS cells the chosen ceramic tube should also have good thermal conductivity. A low cost ceramic material which serves both purposes well is mullite alumina, which unlike silicon carbide (another low cost material that was considered) is electrically non-conductive [86,87]. It is also important to note that for effective heat transfer, the battery tube, ceramic tube and NaS cells must be in good physical contact, albeit within the tolerances allowed for differences in thermal expansion.

Individual NaS cells within the ceramic tube are linked electrically and physically with metallic interconnects, connecting opposite poles (+ with -) of adjacent batteries. Cells in a standard 4 m receiver would be all connected in series. However, practical receiver modules could also be connected in parallel to increase the current capacity of the NaS battery storage system.

To hold the battery tube concentrically within the outer absorber tube, specially designed “end caps” (Figure 4) are either screwed on with appropriate high temperature thread sealant or welded in place at both receiver ends to hold the whole tube assembly together. These end caps have special holes or slots for the passage of HTF into the flow channel, and another channel orthogonal to the HTF flow for feeding the battery cable into the battery.

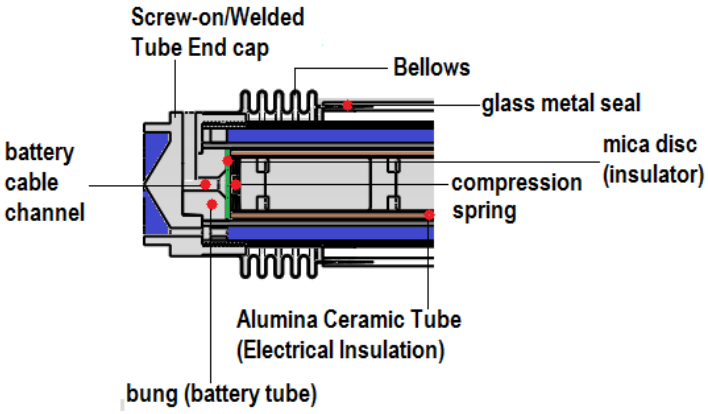

Figure 4: Schematic showing longitudinal section of the EES Receiver near the End Cap

A bung on the inside of each endcap seals the entrance of the battery tube and prevents HTF from entering the battery compartment. Finally, the NaS batteries are electrically insulated from the internal face of this bung and the rest of the receiver body, by a special mica disc. This completes the general description of the components making up the design of conceptual EES receiver, along with their intended functionality. The next section now discusses the intended operation of the designed receiver in a typical PTC Power plant.

4. Operation of the EES Receiver in a typical PTC Power Plant

The EES receiver is intended to operate within a PTC Power plant as the Heat Collecting Element (HCE). A typical PTC power plant layout (Figure 5) comprises three main parts: a solar field, a thermal storage block and a power block. The solar field consists of long rows of highly reflective parabolic trough mirrors, arranged in loops, and attached to large rotatable tracking platforms [88].

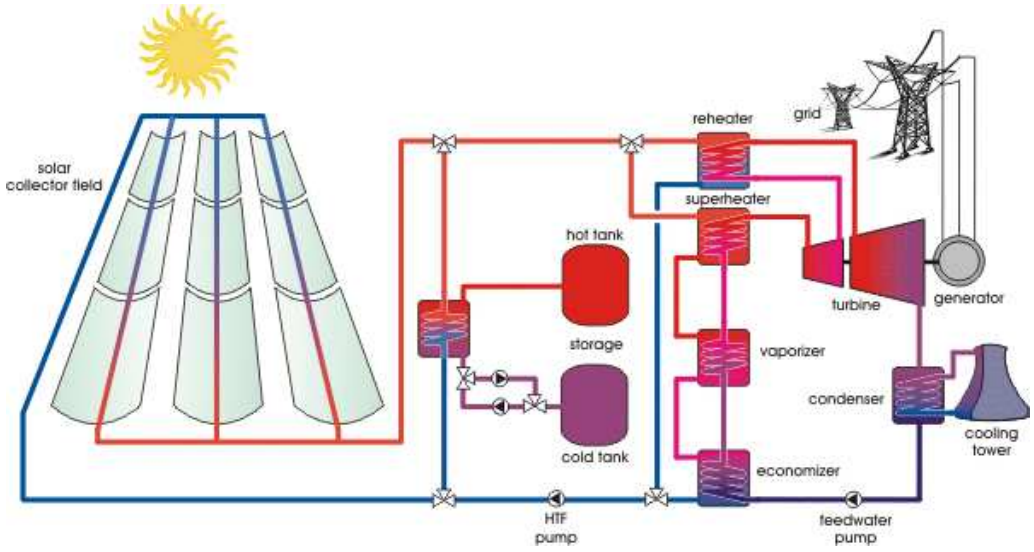

Figure 5: Schematic of layout of a standard PTC Power Plant (Source:[89]**)**

These platforms are oriented axially along a north-south line where they track the sun along an east to west path (Figure 6). Incoming solar "*beam"* radiation is concentrated by a factor of 20 - 80 suns unto a selectively coated black absorber tube, at the focal axis of the trough. Typical solar to electrical conversion efficiencies of 24% [90] are standard for today's commercial PTC plants, a value notably higher than the highest efficiency values (22%) of solar photovoltaic modules available in the market [91].

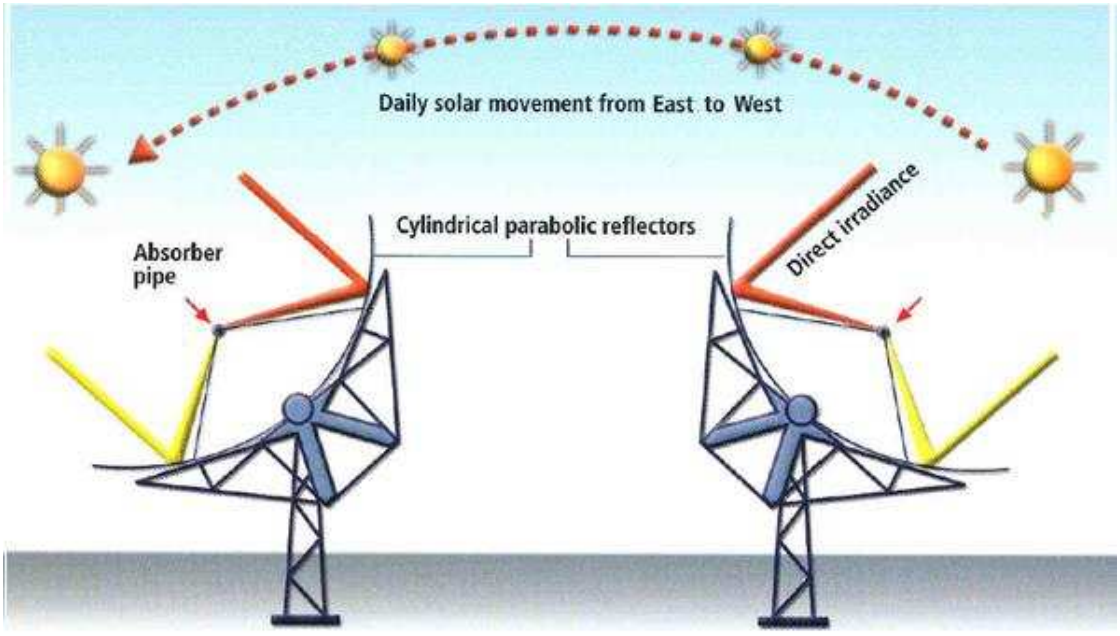

Figure 6: East-West tracking of a parabolic trough collectors (Adapted: [92])

The concentrated solar radiation absorbed by the PTC receiver typically heats a special fluid (HTF) circulating inside (at 8-9 kg/s) up to a working temperature of about 393^{o}C [88]. The hot fluid is then pumped into the plant's power block, where it exchanges sensible heat to produce superheated steam (100 bar, 371^{o}C) for driving a Rankine power cycle steam turbine, which is mechanically coupled to an electric generator [93]. Once through the power block, the cooled HTF is pumped back into the solar field for the cyclic reheating process.

The hybridizing of NaS and PTC technologies to build a conceptual EES PTC power plant is possible because of the following reasons.

a) The 300-400°C operating temperature range of both technologies [6],[3] is naturally coincident.

b) The layout of the conceptual EES PTC plant would be identical to that of an existing PTC power plant, requiring only a special internal modification of the receiver in the solar field.

c) The modification required for production of the EES receiver will affect chiefly the diameter (cross sectional) of the traditional receiver and therefore should adapt itself easily to existing operating facilities.

Some important conditions identified for the operation of this conceptual PTC plant are as follows:

a) The volume of the HTF annulus and/or mass flow in the EES receiver (hence receiver size) must be correctly optimized to maintain the heat transfer/enthalpy requirements of the PTC plant.

b) The HTF mass flow and heat exchange, along with NaS cell charge/discharge must be controlled as required to maintain the NaS cell temperatures ideally within the 300-450°C operating range.

c) The NaS cells should ideally be charged during the main daylight hours, storing available solar energy in electrical form for discharge during evening and night-time hours, when the sun is unavailable and energy demand peaks.

d) In the situation that the cells reach full charge during the daylight hours, the endothermic heat flux normally absorbed during the charging process will become zero. Consequently, if solar flux continues to pass into the cells, cell temperatures could rise above the maximum operating value and cause cell failure. Therefore, HTF mass flows must be controlled such that the temperature of the HTF in the annulus around the cell always stays within the 300-450°C operating range. If this condition is satisfied, the NaS cell temperature will only approach (Figure 7), but never exceed HTF operating temperature range, with flux into the cells becoming zero as $\overline{T}_{NaS} \rightarrow T_{htf}$.

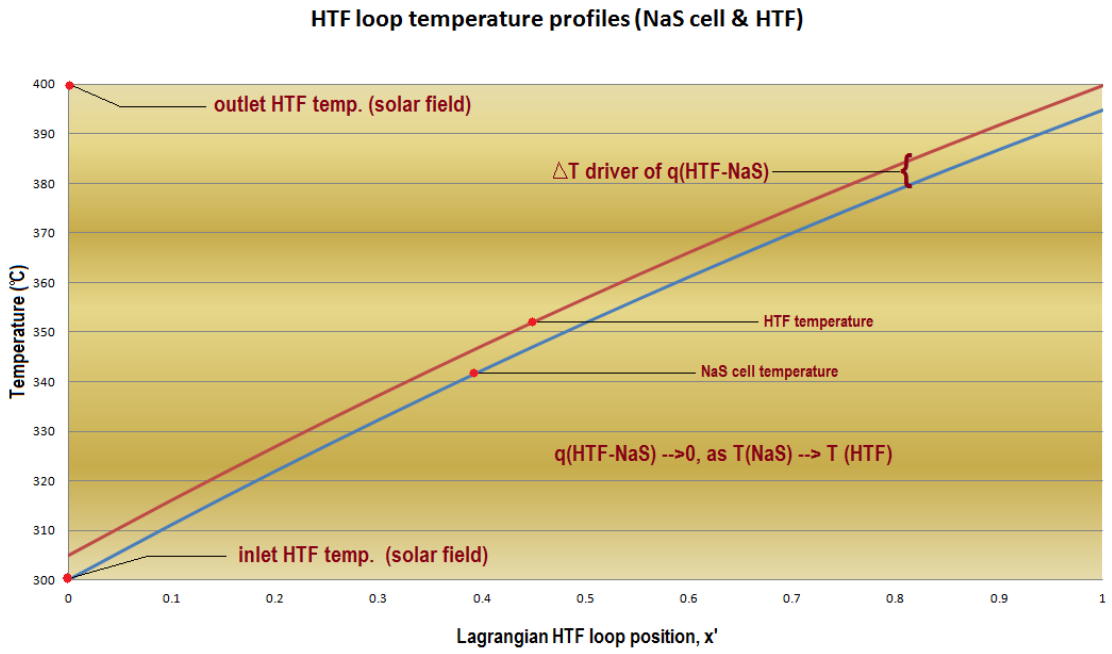

Figure 7: Schematic illustrating the relationship between NaS and HTF temperature profiles

e) Fully charged cells should NOT be discharged for extended periods during daylight hours, since the discharge process is exothermic. However, if this must be done outside of night time hours (eg. to provide ramping reserves and other ancillary power support services), EES receivers should be partially or totally defocused from the incident solar radiation as required to stay within cell operating temperature limits.

In addition, the HTF temperature and mass flow in the EES HTF loop (Figure 8) must be controlled so that the heat generated during cell discharge is sinked from the NaS cells into the power plant block, or into the thermal storage tanks.

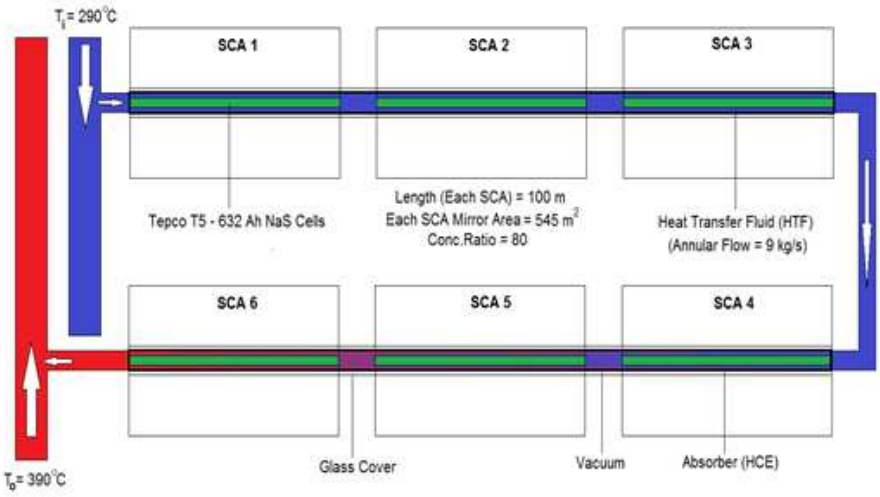

Figure 8: Schematic representation of the conceptual EES HTF loop

Heat transfer in the EES receiver comprises:

a) Heat transfer from the sun to the working fluid

b) Heat losses from the EES receiver to the ambient

c) Heat transfer from the working fluid to the NaS cells

d) Heat transfer from the NaS cells to the working fluid (occurs during electrical discharge)

During daytime hours, solar radiation is used to:

a) Heat the NaS cells in the EES receiver up to a working temperature of between 300°C (HTF inlet temp.) and 400°C (HTF outlet temp.).

b) Raise the HTF up to a typical working temperature of about 400°C for driving the Rankine steam cycle of the power plant.

c) Charge the thermal energy storage system (molten salt tank).

The EES power plant could also provide another very significant advantage over the conventional plant during night time operation. With much lower ambient temperatures, an absence of solar radiation, and possibly clear skies at night time, the temperature of HTF in the solar field will gradually fall and freezing could occur. This is largely owing to heat radiation to the sky and convection to the ambient by the receivers (Figure 9). This problem is solved in conventional PTC plants by circulating the HTF through an auxiliary heat exchanger powered by a gas fired boiler or by electrical joule heating through the absorber tube walls [88].

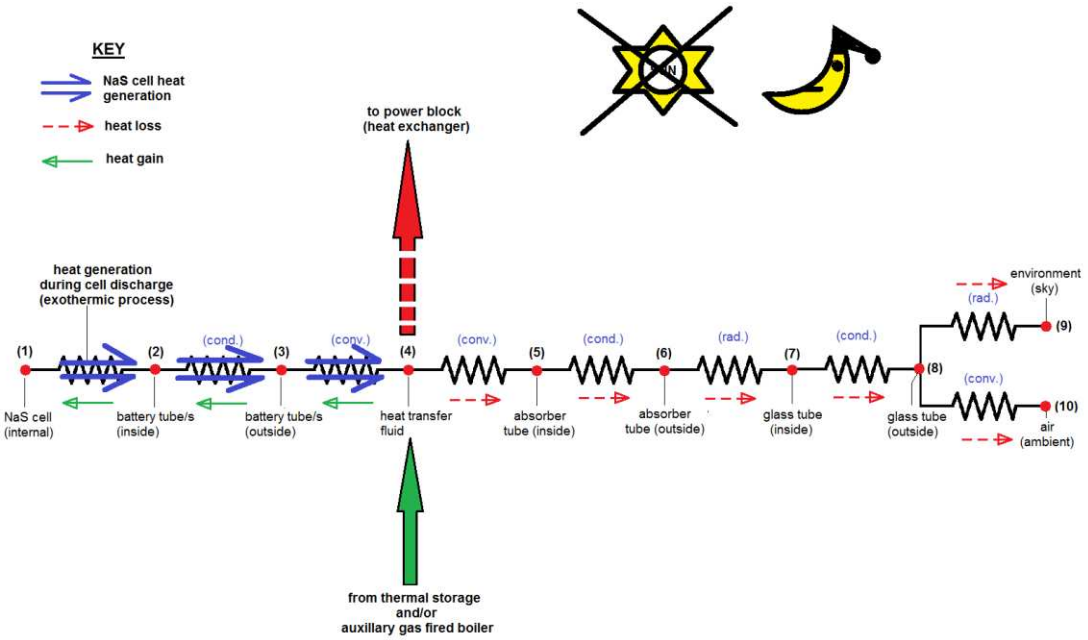

Figure 9: Thermal resistance model of heat flow in the EES receiver (night time)

If the NaS cells are discharged during night time hours for power generation, given that cell discharge is an exothermic process [10], with appropriate controls, the heat generated during night time discharge could prove effective in maintaining the HTF temperature of the solar field, without requiring auxiliary power. All these concepts are topics for future evaluation and thorough analysis. In the next section, the mathematical models describing the heat transfer processes within the EES receiver are presented.

5. Modelling of Heat Transfer to the NaS Cell

In this section, the mathematical models that represent the key heat transfer processes are presented. Assumptions that have been made for the sole purpose of model simplification and easier computation are now given in the brief sub-section that here follows.

5.1. Assumptions used in Heat Transfer Modelling

The following assumptions were made to simplify the system of mathematical equations that model the EES receiver. It was assumed that:

1. A vacuum exists between the absorber tube and glass cover of the EES receiver. Therefore, convective heat loss can be neglected.

2. Conductive losses from the tube supports are negligible and therefore can be ignored.

3. The NaS cells and battery tube combination have infinite conductance, with no axial or radial temperature gradients. Therefore, this allows the use of an average cell temperature $\overline{T}_{NaS}$, in all calculations.

4. Variation in HTF temperature is one-dimensional, and occurs only in the axial (HTF flow) direction. Therefore, the HTF has no radial temperature gradients and an average HTF temperature $\overline{T}_{htf,}$ can be used in all calculations.

5. Both the inner sodium and outer sulphur electrodes change phase at a common temperature representing the solid–liquid phase change temperature for the *"entire NaS cell"*. This greatly simplifies computation and is permissible since the inner sodium electrode (which melts at roughly 100^{o}C) is heated from the outer sulphur electrode which melts at approximately 115.21^{o}C [10],[11]. However, in the simulations presented in section seven, it was more convenient to use a value of 130^{o}C (based on simulated results of HTF outlet temperture).

With the above model assumptions stated, the first modelling sub-section which now follows, presents the lumped capacitance model and the modes of nodular heat transfer within the EES receiver system.

5.2. The NaS Cell Lumped Capacitance Model and Nodular Heat Transfer within the EES Receiver System

For simplicity, but still to provide a useful model of the internal heat transfer, the NaS cell is considered to have infinite internal conductance and lumped thermal capacitance (Figure 10). The actual thermal resistances inside the cell, theoretically considered as being external, are used to calculate an overall heat transfer coefficient $U_{o,NaS}$, between the moving HTF and the NaS cell.

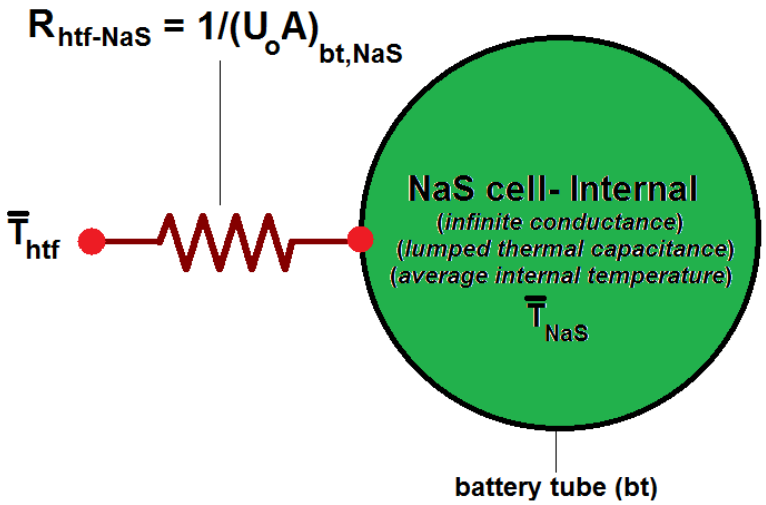

Figure 10: Schematic illustrating lumped thermal capacitance of NaS cell

The calculation of the overall heat transfer coefficient $U_{o,NaS}$ as described by Duffie and Beckman [94] was effected by considering the entire set of layers involved in heat transfer to the NaS cell, as depicted in a simplified longitudinal section of the most widely used *"central sodium"* NaS cell (Figure 11).

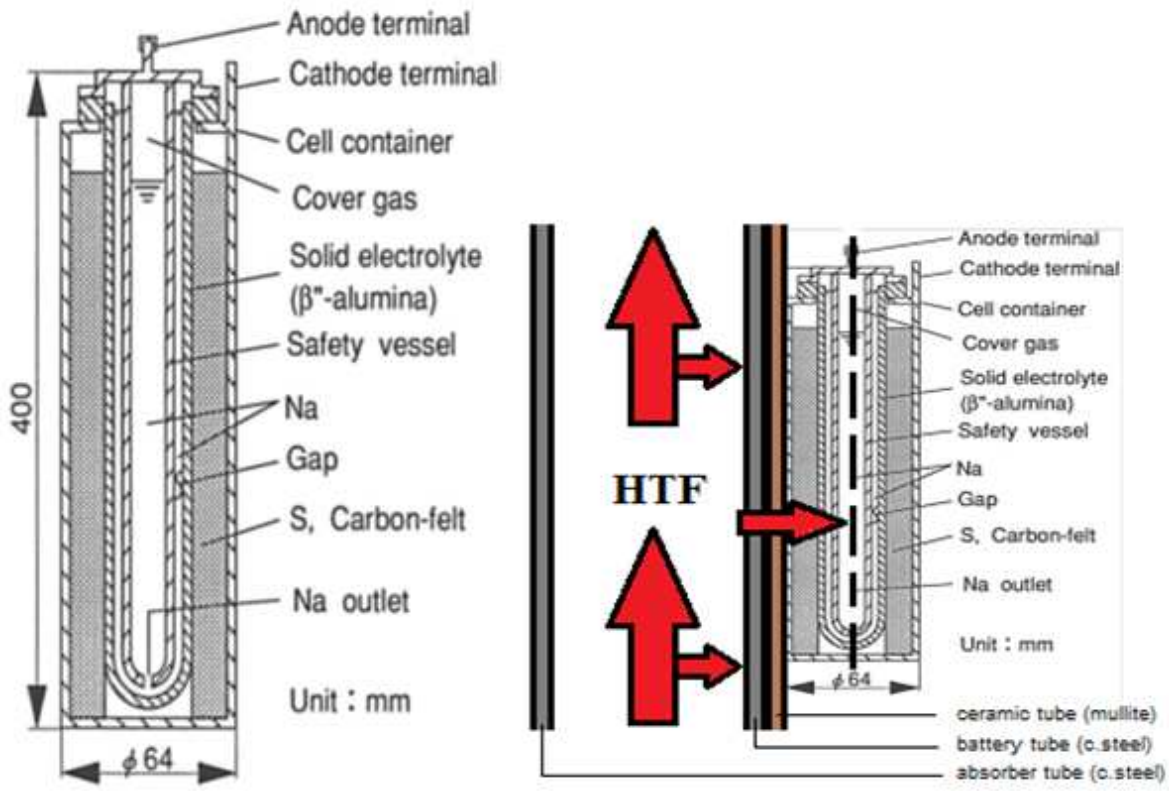

Figure 11: Heat transfer to a 300 Ah central sodium NaS cell (Adapted:[95]**)**

The equation concerning heat transfer to the NaS cell is given as follows:

$$\dot{q}'_{conv,htf-NaS} = U_{o,NaS*}\pi D_{bt,o}(T_{htf} - \overline{T}_{NaS}) \quad (1)$$

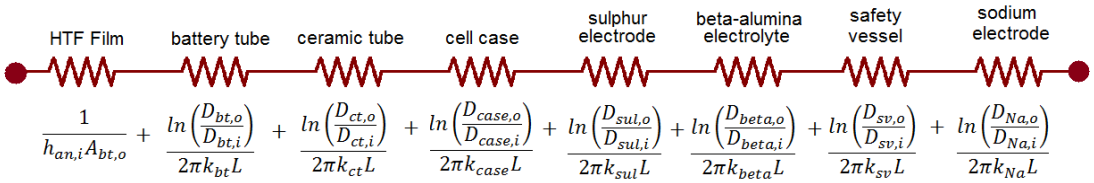

Figure 12: Schematic showing thermal resistance between HTF and NaS Cell

Regarding the resistance network (Figure 12), the overall heat transfer coefficient $U_{o,NaS}$ is given as follows:

$$U_{o,NaS} = \left[\frac{1}{h_{ann,i}} + \frac{D_{bt,o}}{2}\left\{\frac{ln\left(\frac{D_{bt,o}}{D_{bt,i}}\right)}{k_{bt}} + \frac{ln\left(\frac{D_{ct,o}}{D_{ct,i}}\right)}{k_{ct}} + \frac{ln\left(\frac{D_{case,o}}{D_{case,i}}\right)}{k_{case}} + \frac{ln\left(\frac{D_{sul,o}}{D_{sul,i}}\right)}{k_{sul}} + \frac{ln\left(\frac{D_{beta,o}}{D_{beta,i}}\right)}{k_{beta}} + \frac{ln\left(\frac{D_{sv,o}}{D_{sv,i}}\right)}{k_{sv}} + \frac{ln\left(\frac{D_{Na,o}}{D_{Na,i}}\right)}{k_{Na}}\right\}\right] \quad (2)$$

Jefferson (1972) recommended a correction correlation that was used to improve the accuracy of the overall heat transfer coefficient $U_{o,NaS}$ in the lumped capacitance model. It yields a modified coefficient $U_{o,NaS*}$ which brings the results of the lumped capacitance approach into closer agreement (Figure 13) with a transient conduction model. This correlation is given as [96]:

$$\frac{1}{U_{o,NaS*}} = \frac{1+\mathrm{Bi}/5}{U_{o,NaS}} \quad (3)$$

where the Biot number, $\mathrm{Bi} = \frac{U_{o,NaS}L_c}{k_{NaS}}$; and L_c the characteristic length, defined as the ratio of the battery tube's internal volume to surface area is given as:

$$L_c = \frac{Volume_{bt}}{Area_{bt,o}} = \frac{\pi(D_{bt,o})^2/4 \times L_{NaS}}{\pi D_{bt,o} L_{NaS}} = \frac{D_{bt,o}}{4} \quad (4)$$

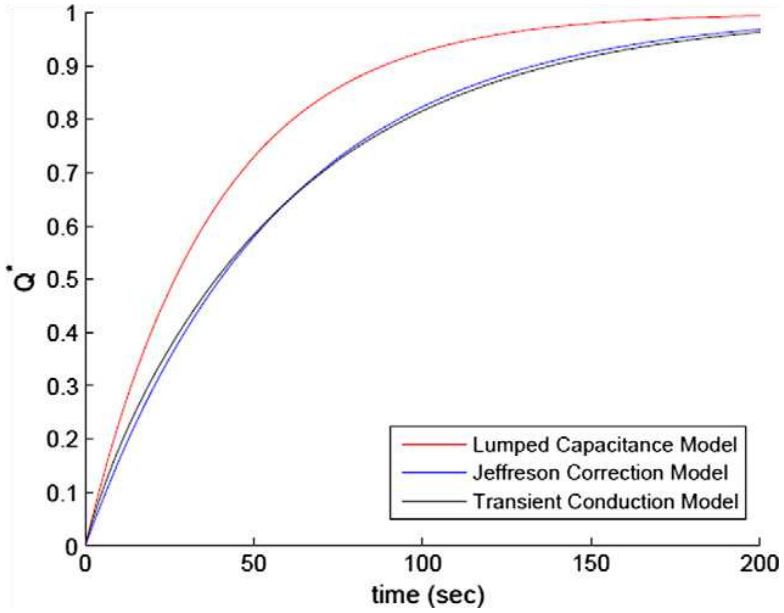

Figure 13: Comparative accuracy of Jefferson's Correction for improving normalized transient heat flux ($\dot{Q}$) predictions in Lumped Capacitance Model predictions (Source: [96]**)**

Time dependent temperature variation in the Tepco T5 NaS cell modelled in this work is due to sensible heat transfer with the HTF, as well as entropic heat generation (exothermic and endothermic during cell discharging and charging respectively) within the NaS cell. As given by

Gibbard (1978), the total heat energy generated or absorbed by the NaS cell can be represented as [97]:

$$\dot{Q}_{NaS} = \dot{Q}_{joule\_heating} + \dot{Q}_{reaction\_entropy} = I_{NaS}\left(\eta - \bar{T}_{NaS}\frac{dE_{NaS}}{d\bar{T}_{NaS}}\right) \quad (5)$$

where η is the battery polarization and $\bar{T}_{NaS}\frac{dE_{NaS}}{d\bar{T}_{NaS}}$ is the entropy term.

The battery polarization $\eta = I_{NaS} \times R_{NaS}$ with R_{NaS}, the internal cell resistance found by the difference between the *"rated"* open circuit voltage at full charge and the cell voltage at a given time *"t"*, all divided by the current flow at that same time.

$$R_{NaS} = \frac{\left(E_{NaS,oc} - E_{NaS,@I_{NaS}}\right)}{I_{NaS}} \quad (6)$$

As stated earlier, it is here assumed that the NaS cell has no axial or radial temperature gradients and that the whole 0.5 m length of the T5 cell is at one common temperature. This simplified approach allows the temperature variation to be time dependent only and represented by the first order partial differential equation given as:

$$\left(\frac{\partial T_{htf}}{\partial x} + \frac{1}{\bar{u}_{htf}}\frac{\partial T_{htf}}{\partial t}\right) = \frac{h_{ann,o}\pi D_{at}\left(T_{at} - T_{htf}\right) + U_{o,NaS}\pi D_{bt,o}\left(\bar{T}_{NaS} - T_{htf}\right)}{\left(\dot{M}c_p\right)_{htf}} \quad (7)$$

$$\frac{\partial \bar{T}_{NaS}}{\partial t} = \frac{h_{ann,i}\pi D_{NaS} l_{NaS}\left(T_{htf} - \bar{T}_{NaS}\right) + I_{NaS}\left(\eta - \bar{T}_{NaS}\frac{dE_{NaS}}{d\bar{T}_{NaS}}\right)}{\left(mc_p\right)_{NaS}} \quad (8)$$

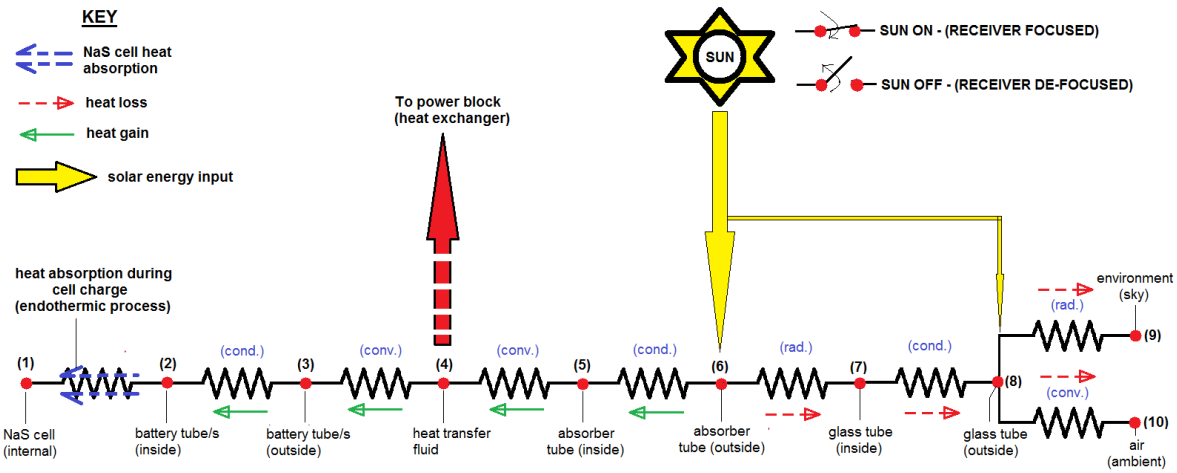

Figure 14: Thermal resistance model of heat flow in the EES receiver (day time)

Here, heat gain from the HTF is given by the $h_{ann,i}$ term and heat generated within the cell during charge/discharge operations by the I_{NaS} and $\frac{dE_{NaS}}{dT}$ terms. The direction of daytime heat flows can be visualized using the thermal resistance network of Figure 14.

At nodes 1-3: (Heat transfer from HTF to NaS Cell)

Since the battery polarization $\eta = I_{NaS} \times R_{NaS}$, Equation (8) can be rewritten as follows:

$$\frac{\partial \overline{T}_{NaS}}{\partial t} = \frac{h_{ann,i}\pi D_{NaS} l_{NaS}(T_{htf} - \overline{T}_{NaS}) + I_{NaS}\left(I_{NaS} \times R_{NaS} - \overline{T}_{NaS}\frac{dE_{NaS}}{d\overline{T}_{NaS}}\right)}{(mc_p)_{NaS}} \quad (9)$$

When only the initial heating of the NaS cells (up to operating temperature) is considered, the current term is zero and the partial differential equation can be simplified as follows:

$$\frac{\partial \overline{T}_{NaS}}{\partial t} = \frac{U_{o,NaS*}\pi D_{bt,o} l_{NaS}(T_{htf} - \overline{T}_{NaS})}{(mc_p)_{NaS}} \quad (10)$$

where $U_{o,NaS*}$, is the overall heat transfer coefficient from the HTF to the NaS cells, developed earlier and modified with the Jefferson correction.

At nodes 3 - 4: (Heat transfer between Battery Tube and HTF)

Like the NaS cell, a uniform HTF temperature is assumed with no radial temperature gradients. In the case of heating the cells to working temperature, heat is expected to flow into the NaS cells from the HTF. However, heat may also flow from the NaS cells into to HTF, during night time or poor sunlight conditions when the NaS battery banks are being discharged.

Therefore, overall battery temperature change may be due to solar heat gain through the inner wall of the absorber tube (given by $\alpha_{ann,o}$), or by heat gained from the NaS cell through the outer battery tube wall (given by $\alpha_{ann,i}$). This is represented in Equation (11) as:

$$\left(\frac{\partial T_{htf}}{\partial x} + \frac{1}{\overline{u}_{\text{htf}}}\frac{\partial T_{htf}}{\partial t}\right) = \frac{h_{ann,o}\pi D_{at}(T_{at} - T_{htf}) + U_{o,NaS}\pi D_{bt,o}(\overline{T}_{NaS} - T_{htf})}{(\dot{M}c_p)_{htf}} \quad (11)$$

Further, the flux conducted through the NaS battery tube wall from the HTF is given by Equation (12 as:

$$\dot{q}'_{cond,bt} = \frac{2\pi k_{bt}(T_{bt,o} - T_{bt,i})}{ln\left[\frac{D_{bt,o}}{D_{bt,i}}\right]} \quad (12)$$

This is the same flux convected from the HTF to the NaS battery tube, and is given by Equation (13 as:

$$\dot{q}'_{conv,htf-bt} = \dot{q}'_{cond,bt} = h_{ann,i}\pi D_{bt,o}\left(T_{htf} - T_{bt,o}\right) \quad (13)$$

At nodes 4-5: (Heat transfer from Absorber Tube to HTF)

At node 4, heat flux enters the HTF by convective heat transfer at the inner wall of the EES absorber tube, being conducted from the outer wall which is focused to concentrated solar flux. This heat flux is given by Equation (14 as:

$$\dot{q}'_{conv,at-htf} = h_{ann,o}\pi D_{at,i}(T_{at,i} - T_{htf}) \quad (14)$$

The heat flux conducted through the absorber tube (node 5 of Figure 14) is equal to the heat flux convected into the HTF and is given by Equation (**15** as:

$$\dot{q}'_{cond,at} = \dot{q}'_{conv,at-htf} = \frac{2\pi k_{at}(T_{at,o} - T_{at,i})}{ln\left[\frac{D_{at,o}}{D_{at,i}}\right]} \quad (15)$$

At nodes 6-7: (Heat balance at the absorber tube)

The heat flux conducted through the absorber tube wall is equal to the solar energy absorbed by the receiver, less the radiative and convective losses at outer surface of the glass cover. This is given by Equation (**16** as:

$$\dot{q}'_{cond,at} = \dot{q}''_{sol.abs,at}\pi D_{at,o} - (\dot{q}'_{Lrad,at-gt} + \dot{q}'_{Lconv,at-gt}) \quad (16)$$

$$\dot{q}'_{cond,at} = \dot{q}''_{sol.abs,at}\pi D_{at,o} - \dot{q}'_{Lrad,at-gt} \text{ since } \dot{q}'_{Lconv,at-gt} = 0. \quad (17)$$

Further:

$$\dot{q}'_{Lrad,at-gt} = \Im_{at,o-gt,i}\sigma\pi D_{at,o}\left(T^4_{at,o} - T^4_{gt,i}\right) \quad (18)$$

and

$$\mathfrak{I}_{at,o-gt,i} = \left[\frac{1}{F_{at,gt}} + \left(\frac{1}{\varepsilon_{at}} - 1\right) + \frac{D_{at}}{D_{gt,i}}\left(\frac{1}{\varepsilon_{gt}} - 1\right)\right]^{-1} \quad (19)$$

The fluxes $\dot{q}'_{Lcond,gt}$ and $\dot{q}'_{sol.abs,gt}$ are given as:

$$\dot{q}'_{Lcond,gt} = \frac{2\pi k_{gt}(T_{gt,i} - T_{gt,o})}{\ln\left[\frac{D_{gt,o}}{D_{gt,i}}\right]} \quad (20)$$

$$\dot{q}'_{sol.abs,gt} = \dot{q}''_{sol.const}\rho_m\gamma_m K_\theta \alpha_{gt}\pi D_{gt,o} \quad (21)$$

At nodes 9-10: (Heat loss from the glass tube to the external environment)

The heat flux conducted through the glass cover is finally lost by radiation to the sky and convection to the ambient (Figure 15). This is represented in Equations 22 to (**24** as follows:

$$\dot{q}'_{Lcond,gt} = \dot{q}'_{Lrad,gt-sky} + \dot{q}'_{Lconv,gt-amb} \quad (22)$$

$$\dot{q}'_{Lrad,gt-sky} = \mathfrak{I}_{gt-sky}\sigma\pi D_{gt,o}\left(T^4_{gt,o} - T^4_{sky}\right) \quad (23)$$

and $\dot{q}'_{Lconv,gt-amb} = h_{conv,gt}\pi D_{gt,o}\left(T_{gt,o} - T_{amb}\right)$ (24)

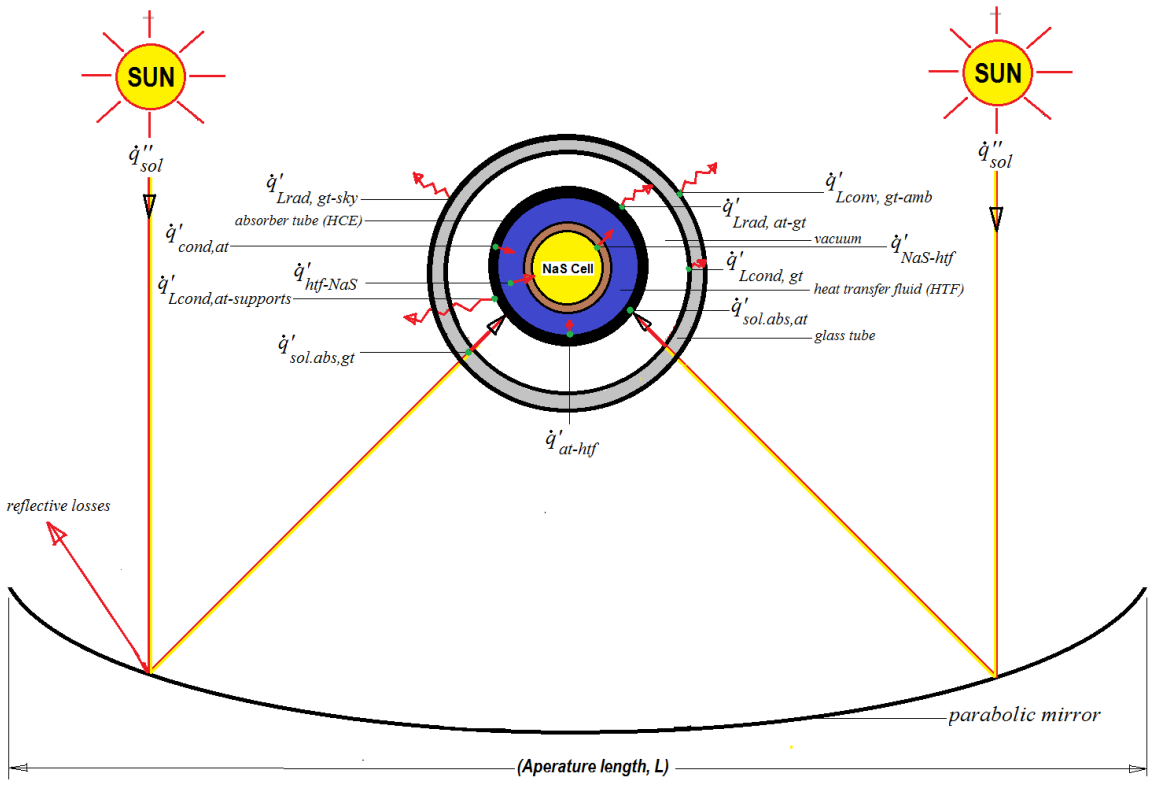

Figure 15: Schematic illustrating the important Heat Fluxes of the EES Receiver

Now that the equations modelling both lumped capacitance and the modes of nodular heat transfer for the EES receiver have been presented, the next sub-section outlines the process developed to solve the key set of steady state algebraic equations just presented.

5.3. Solving the Steady-State System of Equations

Solving the quasi-transient system of equations consisted of a process of precedence ordering and back substitution of the steady state equations to formulate a very nonlinear algebraic equation ((**25**) given in terms of the absorber wall heat flux $\dot{q}'_{cond,at}$. This complex equation was then solved at each spatial node of the model's two discretized transient equations.

Writing $\dot{q}''_{sol.abs,at}$ in terms of the solar constant $\dot{q}''_{sol}$ and optical PTC parameters ($\rho_m, \gamma_m, \tau_{gt}, K_\theta, \alpha_{at}, \alpha_{gt}$), gives:

$$\dot{q}''_{sol}\times CR\times\rho_m\gamma_m\tau_{gt}K_\theta(\alpha_{at}\pi D_{at,o}+\alpha_{gt}\pi D_{gt,o})-\dot{q}'_{cond,at}=$$

$$h_{conv,gt}\pi D_{gt,o}\left(\left[\sqrt[4]{\left\{\frac{\dot{q}'_{cond,at}\times ln\left[\frac{D_{at,o}}{D_{at,i}}\right]}{2\pi k_{at}}+\left[\frac{\dot{q}'_{cond,at}}{h_{ann,o}\pi D_{at,i}}+T_{htf}\right]\right\}^4}-\frac{(\dot{q}''_{sol.const}\times\rho_m\gamma_m\tau_{gt}K_\theta\alpha_{at}\pi D_{at,o}-\dot{q}'_{cond,at})}{\Im_{a,o-gt,i}\sigma\pi D_{at,o}}\right]-\frac{(\dot{q}''_{sol}\times\rho_m\gamma_m\tau_{gt}K_\theta\alpha_{at}\pi D_{at,o}-\dot{q}'_{cond,at})\times\ln\left[\frac{D_{gt,o}}{D_{gt,i}}\right]}{2\pi k_{gt}}-T_{amb}\right)+$$

$$\Im_{gt,o}\pi D_{gt,o}\sigma\left\{\left[\left\{\sqrt[4]{\left\{\frac{\dot{q}'_{cond,at}\times ln\left[\frac{D_{at,o}}{D_{at,i}}\right]}{2\pi k_{at}}+\left[\frac{\dot{q}'_{cond,at}}{h_{ann,o}\pi D_{at,i}}+T_{htf}\right]\right\}^4}-\frac{(\dot{q}''_{sol}\times\rho_m\gamma_m\tau_{gt}K_\theta\alpha_{at}\pi D_{at,o}-\dot{q}'_{cond,at})}{\Im_{a,o-gt,i}\sigma\pi D_{at,o}}\right\}-\frac{(\dot{q}''_{sol}\times\rho_m\gamma_m\tau_{gt}K_\theta\alpha_{at}\pi D_{at,o}-\dot{q}'_{cond,at})\times\ln\left[\frac{D_{gt,o}}{D_{gt,i}}\right]}{2\pi k_{gt}}\right]^4-T_{sky}^4\right\} \quad (25)$$

This is the central implicit and non-linear equation in terms of useful heat flux through the absorber tube walls into the HTF, $\dot{q}'_{cond,at}$ that is the backbone of all model computations. The goal seek tool in Microsoft Excel was employed to find the value of this heat flux at each spatial node of the computational domain.

To corroborate the accuracy of the MS Excel results, a binary search (see supplementary data in the supporting files accompanying this paper) was conducted to check the MS Excel output. Both results agreed and the resulting values were identical to a tolerance of 10^{-4}. With $\dot{q}'_{cond,at}$ computed, the other fluxes and temperatures across the cross section (which are functions of $\dot{q}'_{cond,at}$) were easily determined. The next sub-section outlines the reference frame transformation for the two partial differential equations used in the model.

5.4. Reference Frame Transformation for the Transient Equations of the Heat Transfer Model

The second step in the process of solving the system of equations was the transformation of the transient Equations (**26** and (**27** from a Eulerian to a Lagrangian flow reference frame.

$$\left(\frac{\partial T_{htf}}{dx}+\frac{1}{v_{\mathrm{htf}}}\frac{\partial T_{htf}}{\partial t}\right)=\frac{h_{ann,o}\pi D_{at}\left(T_{at}-T_{htf}\right)+h_{ann,i}\pi D_{bt}\left(\overline{T}_{NaS}-T_{htf}\right)}{\left(\dot{M}c_p\right)_{htf}} \quad (26)$$

$$\frac{\partial \overline{T}_{NaS}}{\partial t}=\frac{h_{ann,i}\pi D_{NaS}l_{NaS}\left(T_{htf}-\overline{T}_{NaS}\right)+I_{NaS}\left(I_{NaS}R_{NaS}-\overline{T}_{NaS}\frac{dE_{NaS}}{d\overline{T}_{NaS}}\right)}{\left(mc_p\right)_{NaS}} \quad (27)$$

The transformed equations (28 and (29 are:

$$\frac{\partial \overline{T}_{NaS}}{\partial t'}|_{x'}=\frac{h_{ann,i}\pi D_{NaS}L'_{NaS}\left(T_{htf}-\overline{T}_{NaS}\right)}{\left(mc_p\right)_{NaS}} \quad (28)$$

$$\frac{\partial T_{htf}}{\partial x'}|_{t'}=L_{flow\ loop}\times\left\{\frac{h_{ann,o}\pi D_{at}\left(T_{at}-T_{htf}\right)+h_{ann,i}\pi D_{at}\left(\overline{T}_{NaS}-T_{htf}\right)}{\left(\dot{M}c_p\right)_{htf}}\right\} \quad (29)$$

The discretization of the P.D.E's for numerical solution using a finite differences approach is given next.

5.5. Discretization and Numerical Solution of the Partial Differential Equations

The transformed P.D.E's ((**28**) and ((**29**), were discretized for solution by a finite differences numerical scheme comprising a first order forward difference (predictor), and a second order modified central difference (corrector).

Using the forward difference predictor, the HTF partial derivative was re-written as follows:

$$\frac{\partial T_{htf}}{\partial x'}|_{t'}=\frac{T_{htf_{i+1}}-T_{htf_i}}{\Delta x'} \quad (30)$$

and

$$\frac{\partial \overline{T}_{NaS}}{\partial t'}|_{x'}=\frac{\overline{T}_{NaS_{i+1}}-\overline{T}_{NaS_i}}{\Delta t'} \quad (31)$$

At the first increment i = 1 using the first order predictor:

$$\boldsymbol{T_{htf(1)} = T_{htf(0)} + \Delta x' \times L_{flow\ ch.}} \left[\frac{\alpha_{ann,o}\pi D_{at}(T_{at}-T_{htf})+\alpha_{ann,i}\pi D_{at}(\bar{T}_{NaS,initial}-T_{htf})}{(\dot{M}c_p)_{htf}}\right]_0 \quad (32)$$

Modifying this result using the second order corrector gives:

$$\boldsymbol{T'_{htf(1)} = T_{htf(0)} + \frac{\Delta x' \times L_{flow\ ch.}}{2}} \left\{\left[\frac{h_{ann,o}\pi D_{at}(T_{at}-T_{htf})+h_{ann,i}\pi D_{at}(\bar{T}_{NaS}-T_{htf})}{(\dot{M}c_p)_{htf}}\right]_0 + \left[\frac{h_{ann,o}\pi D_{at}(T_{at}-T_{htf})+ h_{ann,i}\pi D_{at}(\bar{T}_{NaS}-T_{htf})}{(\dot{M}c_p)_{htf}}\right]_1\right\} \quad (33)$$

Programme code for a Visual Basic code was written in Microsoft Excel to implement the numerical solution of this "quasi-transient" system of equations. The predictor and corrector calculations were iterated until the difference between predicted and corrected values was within a given tolerance of 1x 10^{-4}°C. The value of the absorber tube temperature used in these calculations was derived from the solution (using a Microsoft goalseek tool) of the precedence ordered highly non-linear equation (**25**) given in terms of the heat flux $\dot{q}'_{cond,at}$.

The other transient equation (34) regarding the sodium sulphur battery temperature $\bar{T}_{NaS}$, was solved analytically at the same increment using the *"final corrected value"* of HTF temperature obtained from the finite difference approximation to the solution.

$$\frac{\partial \bar{T}_{NaS}}{\partial t'}|_{x'} = \frac{h_{ann,i}\pi D_{bt,o}L'_{NaS}(T_{htf}-\bar{T}_{ssc})}{(mc_p)_{ssc}} \quad (34)$$

Since x' is invariant at $(0, t')$, then Equation (34 becomes the ordinary differential Equation (35:

$$\frac{d\bar{T}_{NaS}}{dt'} = \frac{h_{ann,i}\pi D_{bt,o}L'_{NaS}(T_{htf}-\bar{T}_{NaS})}{(mc_p)_{NaS}} \quad (35)$$

This equation was solved by separation of variables at $(x, t') = (0, t'_1)$ to obtain the following solution:

$$\bar{T}_{NaS}|_{0,t'_1} = T_{htf}|_{0,t'_0} + \left(\bar{T}_{NaS(0,t'_0)} - T_{htf}|_{0,t'_0}\right)\exp^{-(At'_1)} \quad (36)$$

where the time value at the next increment is given as:

$$t'_1 = \frac{\Delta x}{u_{htf}} - t_0 \,. \quad (37)$$

Since $t_0 = t'_0$, then also:

$$\boldsymbol{t'_1 = \frac{\Delta x}{u_{htf}} - t'_0} \quad (38)$$

For $(x', t') = (0, t'_1)$, both C and $T_{htf(0,t'_1)}$ are evaluated using the properties of the HTF and NaS cell coded into the MS Excel macro at $(x', t') = (1,0)$.

With this solution of the average cross sectional NaS cell temperature $\bar{T}_{NaS}$, all the temperature profiles along the EES receiver length are now defined. Thus, the full mathematical model of the system has been presented. Although this model does assume an average temperature for both HTF and NaS cells in all computations performed, it still provides useful insights into the nature of the expected heat transfer processes during the operation of the conceptual EES receiver.

6. Model Validation

Heat transfer in the EES receiver is composed primarily of two *"useful energy"* producing processes: (a) heat transfer to the HTF and (b) heat transfer to the NaS batteries. It is the second aspect of this heat transfer process that constitutes the fundamental difference between this current model and all the other PTC receiver models developed to date.

Despite this difference however, it is still possible to compare the outputs of the EES receiver model with both credible PTC test data and with recognized models of key researchers. This can be achieved if the NaS cells are modelled and held under adiabatic conditions (at ambient temperature) so that useful solar energy is transferred only to the HTF, as in the case of a standard PTC receiver.

By the process of setting the inner annular heat transfer co-efficient (for the NaS cells) to zero, changing the outer annular diameter to the standard internal diameter of a typical PTC receiver tube and making the inner one infinitesimally small, the required comparisons were realized.

Four key performance metrics of the conceptual EES solar receiver were evaluated, namely:

a) Receiver heat loss per metre length with absorber temperature

b) Collector efficiency with HTF temperature

c) Useful energy gain of the HTF with temperature

d) Tube temperature with loop position in metres

Forristall [98] and Dudley [99] are both prominent researchers in the field who have modelled the heat transfer processes in commercial PTC receivers. Forristall developed numerical 1-D and

2-D models which were solved in Engineering Equation Solver [100]. Dudley's model on the other hand was one dimensional and analytical.

Of the two models, the Forristall model [101] was chosen for most of the comparative simulations performed, as the simulation parameters used were the most explicit. The following operating conditions, as reported in the work of Forristall were used in all validation simulations:

- DNI (Direct normal insolation) = 950 W/m^2
- HTF = Therminol VP-1 @ 2.58 m/s
- Collector = LS-2
- Receiver = Schott PTR-70
- T_{sky} =14°C ; T_{amb} = 22°C

- **Validation Result 1 - Receiver Heat Loss per metre length (W/m)**

In the first comparison, the EES model was used to simulate heat loss characteristics of a receiver with physical dimensions like that of a standard PTC receiver and compared against National Renewable Energy Laboratory (NREL), USA test data. Consequently, the model predicted EES receiver heat loss, as a function of absorber temperature is plotted in Figure 16, along with experimental data obtained from test results conducted at the National Renewable Energy Laboratory (NREL) USA. These test results were obtained from NREL test reports written by Burkholder and Kutscher[102],[103].

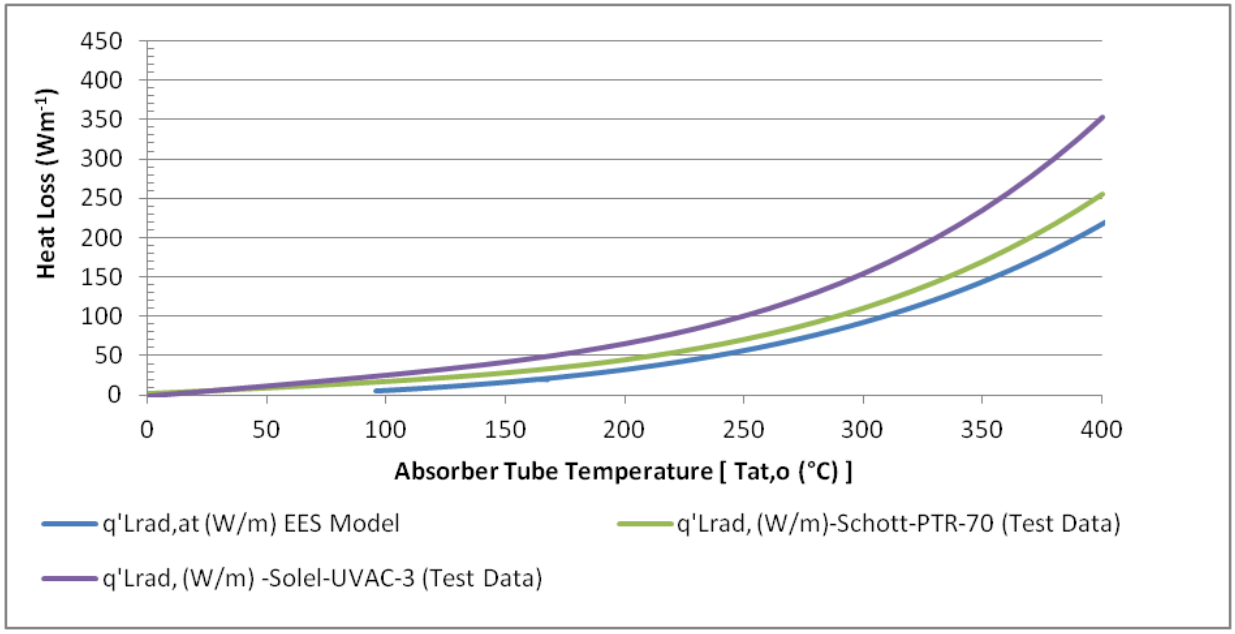

Figure 16: Absorber heat loss per metre length vs. absorber tube temperature

It was observed that the EES model under predicts the actual absorber heat loss. This results from the fact that it assumes a perfect vacuum between absorber and glass tubes, thus ignoring the convective heat exchange in the annulus. However, of the two receivers, test results of the high-quality Schott PTR-70 most closely approximated those of the idealized condition predicted by the EES receiver model.

- **Validation Result 2 - Collector Efficiency with HTF Temperature above Ambient**

The collector efficiency output of the model was compared with validated models and experimental data of researchers Forristall [98] and Dudley[99]. Like the Forristall model, the EES model used Therminol VP-1 as the circulating HTF, and simulated performance under similar operating conditions. As expected, the EES model predicted slightly higher collector efficiency for the same operating temperature, because of the ignored heat losses previously mentioned.

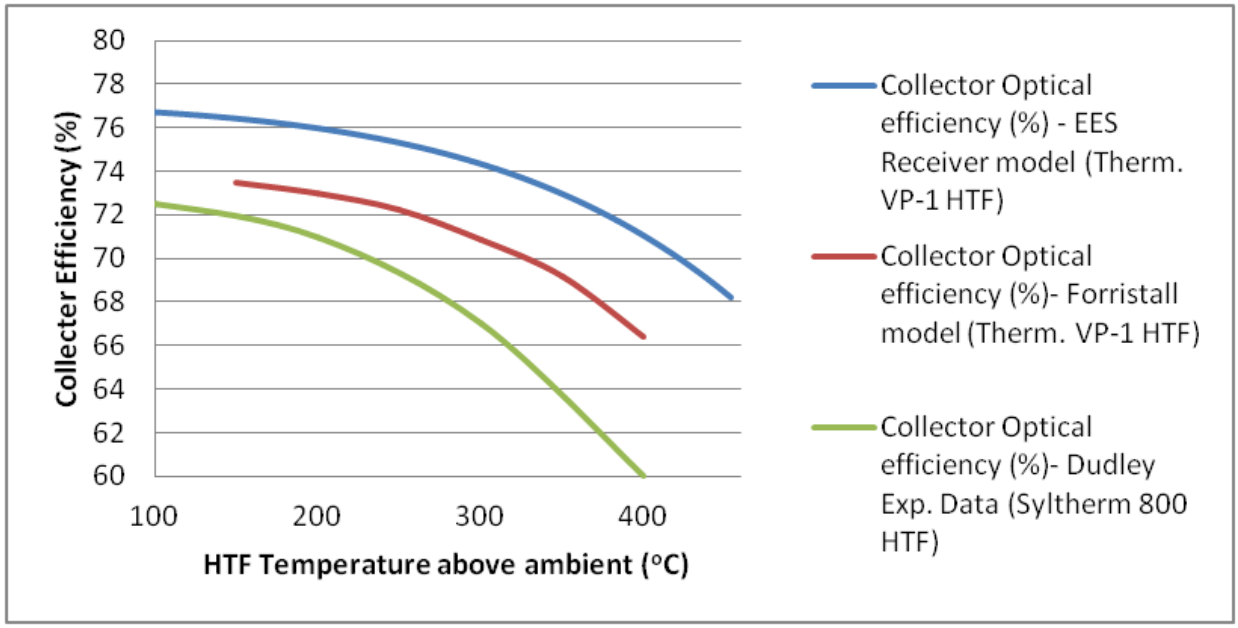

Figure 17: Collector efficiency vs. HTF temperature above the ambient (°C)

However, the efficiency curve can be seen to follow the general shape of the Forristall model by a fixed value of approximately 5-6 % (Figure 17) owing primarily to the fact that the same HTF was modelled in both cases. The efficiency *"fall-off"* in the experimental data reported by Dudley [99] however, differed from the other two curves. This resulted from the fact that Syltherm 800 HTF was instead used and the tests conditions were also slightly different.

- **Validation Result 3 - Useful Energy Gain of the HTF**

The useful energy gain of the HTF with operating temperature along with the 1D model of Forristall [98] is given in Figure 18. The EES model also over predicts the useful energy gain due to the ignored losses stated earlier *(convective heat loss between absorber tube and glass cover and the conductive heat loss from the tube support points along the receiver tube length)*.

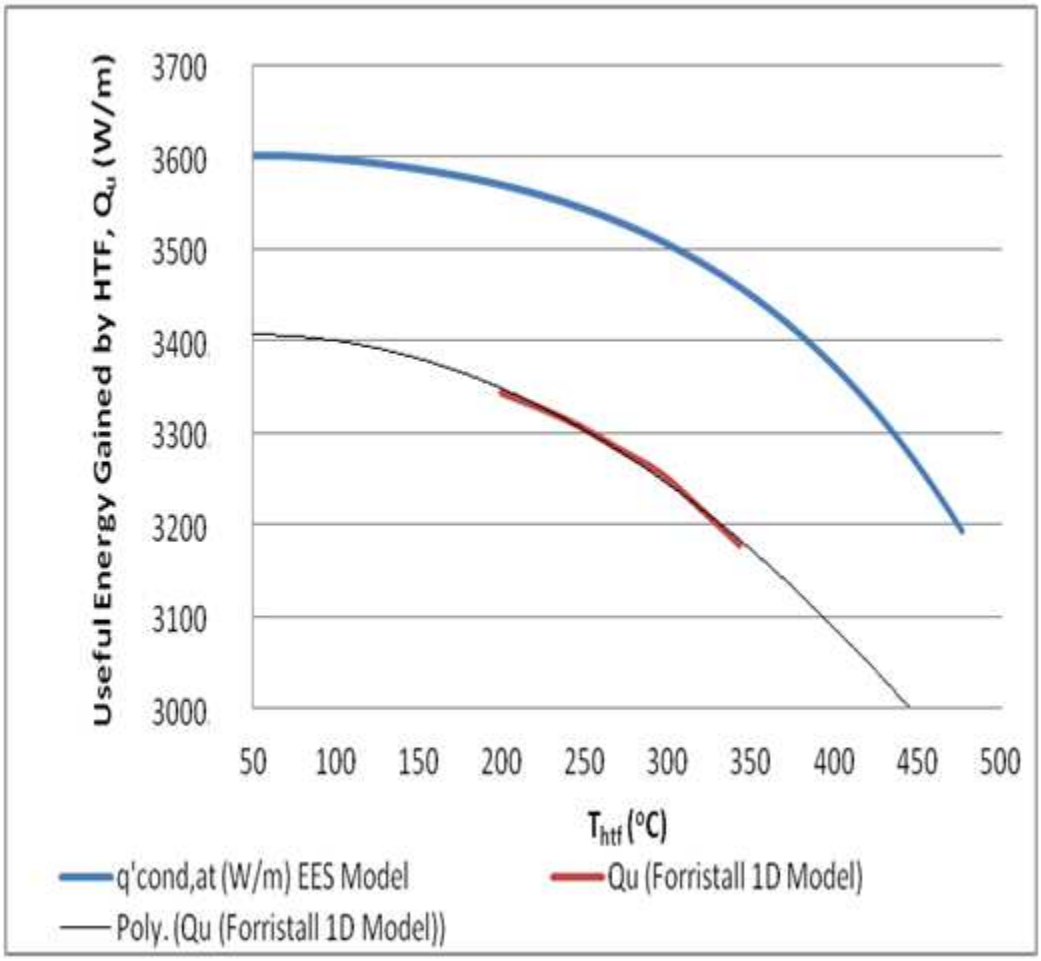

Figure 18: Useful energy gain of the HTF with operating temperature

Although Forristall's model simulated performance over only a small temperature range, the EES model curve nevertheless follows the general trend of the Forristall model (Figure 18) but exceeds each value by approximately 200 W/m. This value is representative of the combined heat losses (convective and conductive) per metre length of receiver, ignored by EES receiver model and gives a rough idea of the magnitude of these losses.

- **Validation Result 4 - HTF Temperature Profile along Flow Loop**

The final and most critical validation concerned the HTF temperature profile along the flow loop as predicted by the EES receiver model. This EES receiver model results of this work were compared with the predicted profile of the Forristall 2-D model [98] by setting the inner heat transfer coefficient of the NaS cell to zero. Results revealed that the EES temperature profile very

closely followed the Forristall model at lower operating temperatures (Figure 19) but slightly over predicted the final HTF outlet temperature.

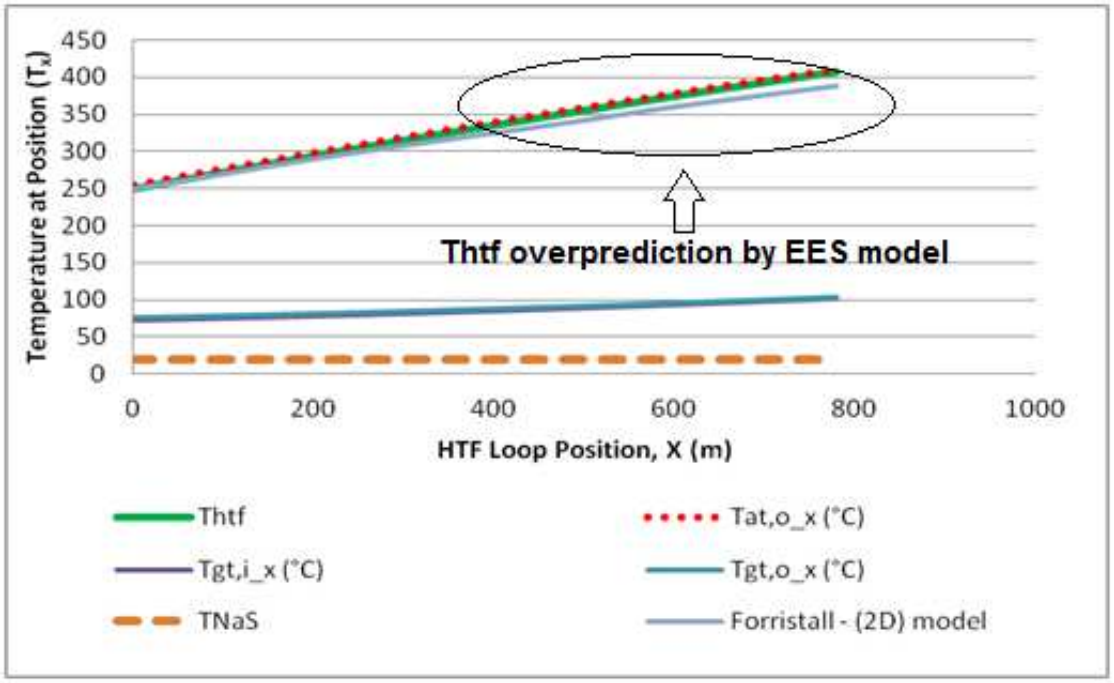

Figure 19: Simulated tube temperature profiles with HTF loop position

Based on the results of the comparative simulations, the EES model has been shown to closely replicate the model predictions of other key researchers and of valid NREL test data, albeit from an idealized perspective. This is suggestive of general model reliability for simulating the theoretical performance of the conceptual EES solar field. It has been deduced that the EES model over predicts solar field efficiency by roughly 5-6% and that a predicted useful energy gain of between 3200 – 3600 W/m (over the 0 - 400^{o}C operating range) contained an ignored heat loss in the range of 40 - 200 W/m (for all compared data). From results, it was observed that at maximum temperature of 450 ^{o}C the EES model (when compared to data from the state of the art SCHOTT PTR-70 receiver) under-predicted heat loss by a maximum of 15% due to the accumulated error from model idealization accumulated over the computational domain.

6.1. Model Set-up Parameters and Properties used in Simulations

The simulation parameters used in the EES receiver model are given below in Table 2. The EES receiver dimensions are those mentioned in the previous section and the solar field specifications are like those of the Andasol-1 PTC power plant at 18514 Aldeire, Granada, Spain.

Table 2: Model parameters used in EES Receiver solar field simulation

EES Receiver solar field model property (Unit)	Value
Absorber tube outer diameter, [wall] (m)	0.168, [0.007]
Glass tube outer diameter, [wall] (m)	0.190, [0.005]
NaS battery tube outer diameter, [wall] (m)	0.114, [0.006]
HTF annulus diameter, (m)	0.040
HTF loop length, (m)	576
Number of HTF loops	156
Tepco - T5 NaS cell diameter, (m)	0.0916
Specific Heat Capacity: Tepco - T5 NaS Cell	744.2 J/kg.K **[EES model calc.]**
Therminol VP-1 HTF mass flow (kg/s)	3-9
HTF inlet temperature (°C)	20
Initial NaS battery temperature (°C)	20
Ambient temperature (°C)	(SEGS VI data file, July 11, 1991)
Sky Temperature (°C)[85]	$0.05525 \times T_{amb}{}^{1.5}$
Start-up time of day	6:30 am
(Latitude, Longitude)- SEGS Solar Plants, USA- ***[Used for weather data]***	(35°N, 117°W)

EES Receiver solar field model property (Unit)	Value
(Latitude, Longitude)- 50 MW_e Andasol-1 Solar Plant, Granada, Spain *[Used for solar field specifications in this model]*	(37°N, 73°W)
DNI @ start-up (W/m^2)	(SEGS VI data file, July 11, 1991)
Flux concentration ratio	12.37
Receiver incidence angle	0°
Collector/receiver parameters $\tau, \alpha, \rho, \varepsilon, \gamma, K_\theta$ ***(transmittance, absorbance, reflectivity, emissivity, mirror shape factor, and incidence angle modifier respectively)***	$\tau_{glass} = 0.97;\ \alpha_{at} = 0.98;\ \alpha_{gt} = 0.03;\ \rho_{mirror} = 0.9;$ $\varepsilon_{at}\ (correlation)^9;\ \varepsilon_{gt} = 0.9;\ \gamma = 0.9;\ K_\theta = 1$
Collector types applicable for comparison in this model	LS-3, E-100, E-150

One of the set-up parameters listed in Table 2, identified the industry standard Therminol VP-1, as the HTF chosen for simulation. The temperature dependent fluid properties for this HTF [104] are given as follows:

$$\boldsymbol{\lambda_{Therminol\,VP-1}} = 0.137743 - 8.19477\times10^{-5}\left(T_{htf}\right) - 1.92257\times10^{-7}\left(T_{htf}\right)^2 + 2.5034\times10^{-11}\left(T_{htf}\right)^3 - 7.2974\times10^{-15}\left(T_{htf}\right)^4 [\mathrm{W/mK}]$$

$$\boldsymbol{c_{p_{Therminol\,VP-1}}} = 1498 + 0.002414\times\left(T_{htf}\right) + 5.9591\times10^{-6}\left(T_{htf}\right)^2 - 2.9879\times 10^{-8}\left(T_{htf}\right)^3 + 4.4172\times10^{-11}\left(T_{htf}\right)^4 [\mathrm{J/kg.\,K}]$$

$$\boldsymbol{\rho_{Therminol\,VP-1}} = 1083.25 - 0.90797\times\left(T_{htf}\right) + 0.00078116\times\left(T_{htf}\right)^2 - 2.367\times 10^{-6}\left(T_{htf}\right)^3 [\mathrm{kg/m^3}]$$

$$\boldsymbol{\nu_{Therminol\,VP-1}} = e^{\left(\frac{544.149}{(T_{htf})+114.43} - 2.59578\right)}\times10^{-6} [\mathrm{m^2/s}]$$

Finally, both the NaS cell and Parabolic Trough Collector used in the model simulations is illustrated in Figure 20. This couple comprised the Tepco-T5 1.22kWh NaS cell and the commercially deployed LS-3 type Parabolic Trough Collector.

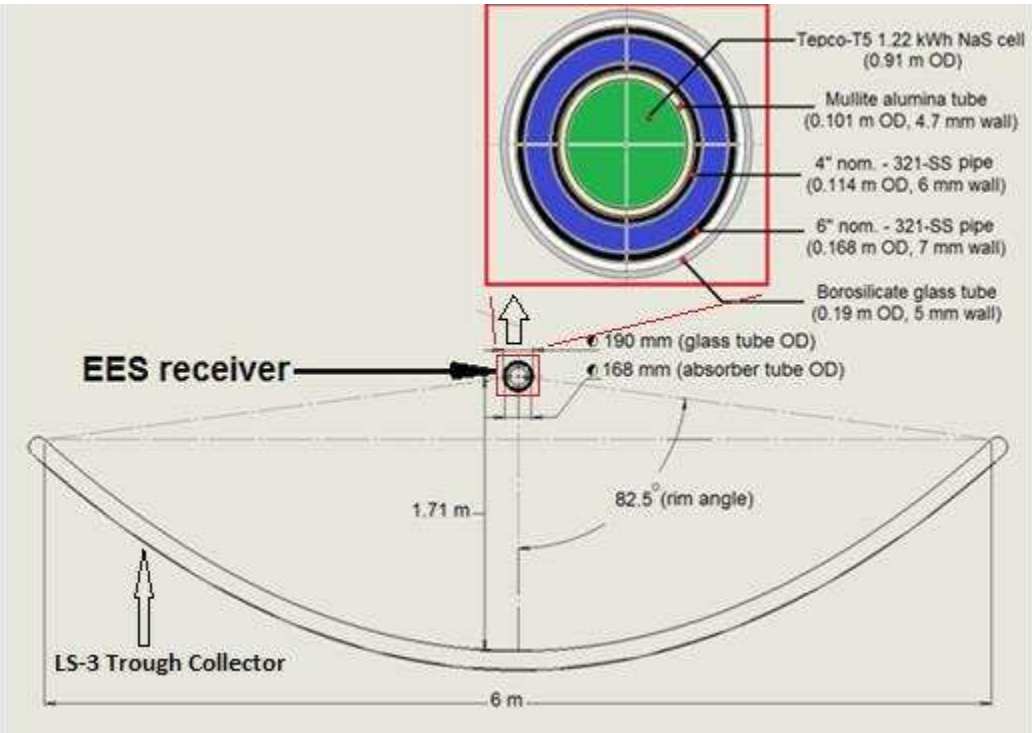

Figure 20: Collector and NaS Cell dimensions used in simulation of the EES Receiver solar field

The section which follows next presents results obtained for model simulations describing the initial heating up of a typical 50 MWe Andasol-1 type sola field with integrated EES receivers.

7. Results from Simulations for the Initial Heating of a Conceptual 50 MWe Solar Collector Field utilizing the EES Receiver

Real operational simulations for the initial heating up of the solar field were approximated using the weather data obtained for the SEGS VI power plant, at Kramer Junction, California on July 18, 1991 (shown in Figure 21).

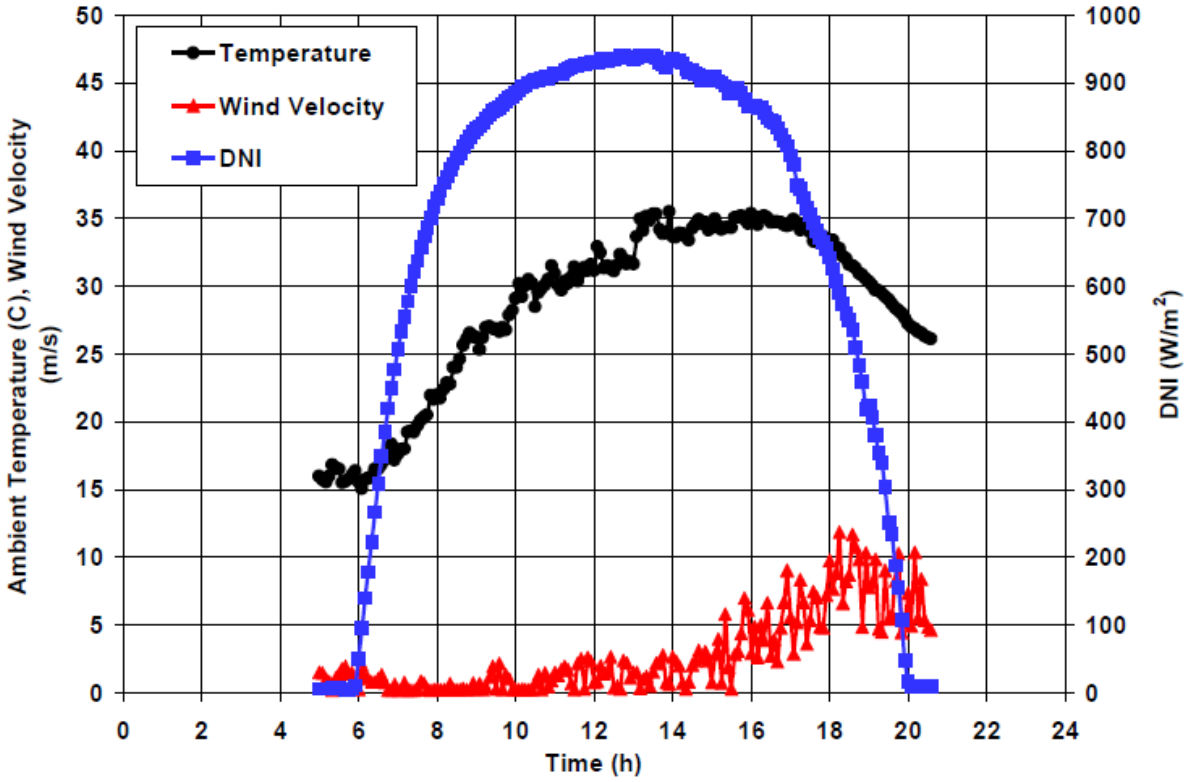

Figure 21: Weather data at SEGS VI power plant, Kramer Junction, California on July 18, 1991 (Source:[105]**)**

For the model start-up, NaS battery temperatures along the HTF loop were held at their initial cold temperature of 20°C. This is referred as the *"zero pass"* through the system (Figure 22). The HTF was thus allowed to heat up as it flows through the loop at a relatively low mass flow of 2.5 kg/s, a value chosen to reduce the pumping power expended during initial heating and at the same time allow a HTF temperature rise above 100°C. Model results predicted an exit temperature of 140°C, or a temperature rise of 120°C. This value is close to the standard temperature rise of 100°C, typical of all solar fields operating with synthetic oil, at fully rated mass flows.

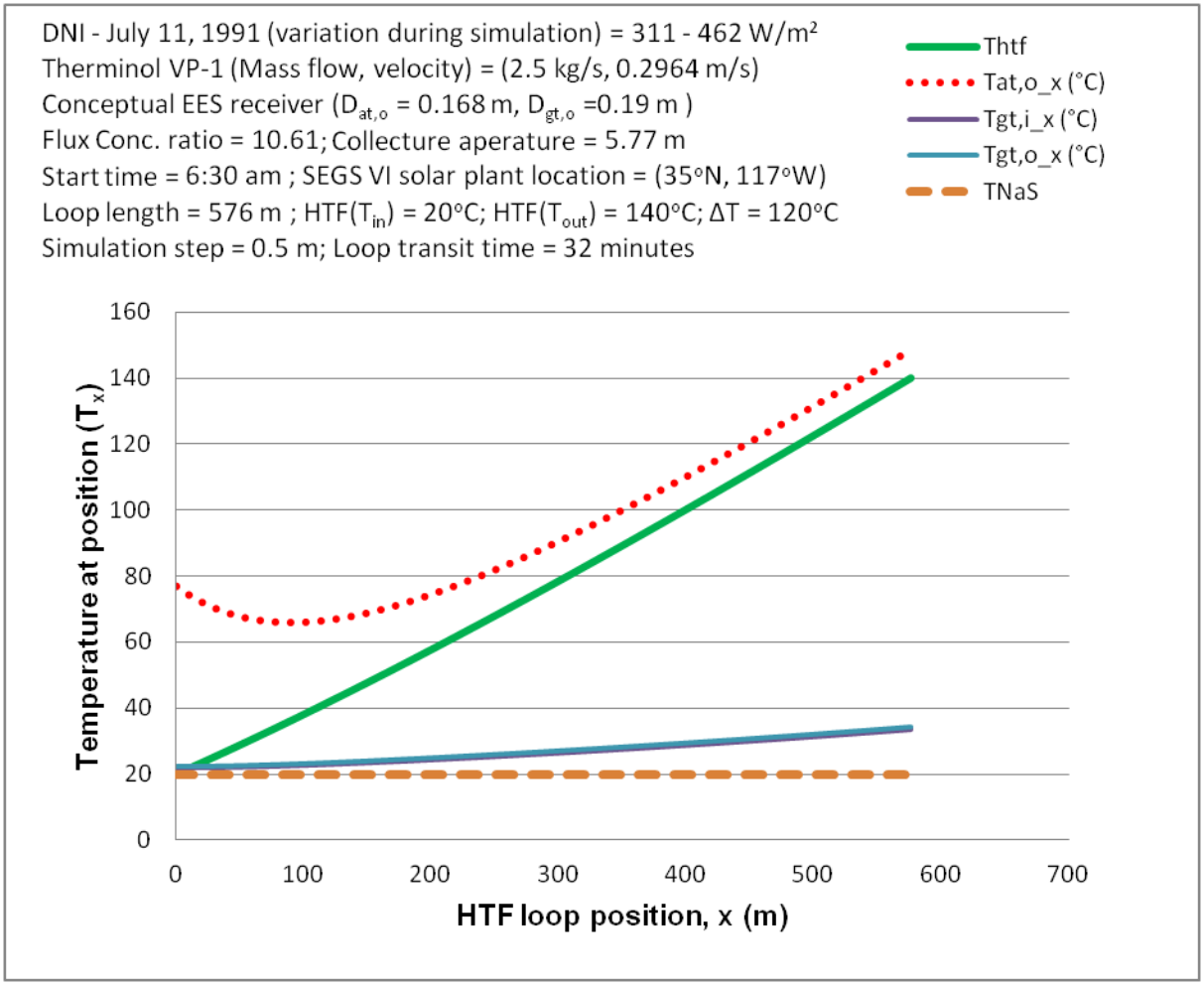

Figure 22: Temperature profiles during the "zero pass" through the HTF loop

After the *"zero"* pass was used to establish the initial temperature profile of the HTF, heat transfer was thereafter allowed with the NaS cells during on the *"first pass"* of the HTF through the loop. As expected, heat transfer to the NaS cells resulted in a slight fall in HTF temperature (≈130°C) when compared to the outlet temperature of the *"zero pass"* profile (140°C).

This fall would have been greater had it not been for the relatively high series internal thermal resistance of the NaS cells, a value largely influenced by the thermal resistances of the sulphur electrode (0.205 W/mK) and β-alumina electrolyte (3 W/mK) respectively [10].

Another important observation is the large difference (Figure 23) between the absorber tube and HTF temperatures at start-up. This large difference results from the impact of concentrated solar radiation on an initially cold absorber tube, and the time delay in effecting heat transfer to the

HTF (absorber thermal inertia). It was also seen that this difference is significantly reduced as the HTF heats up along the HTF flow path.

The glass cover temperature change was seen to be nonlinear, but is at a significantly lower value compared to the NaS and HTF temperatures. Also, owing to incident concentrated solar radiation passing *"into"* the receiver, the outer glass surface was seen to be slightly hotter than the inner one.

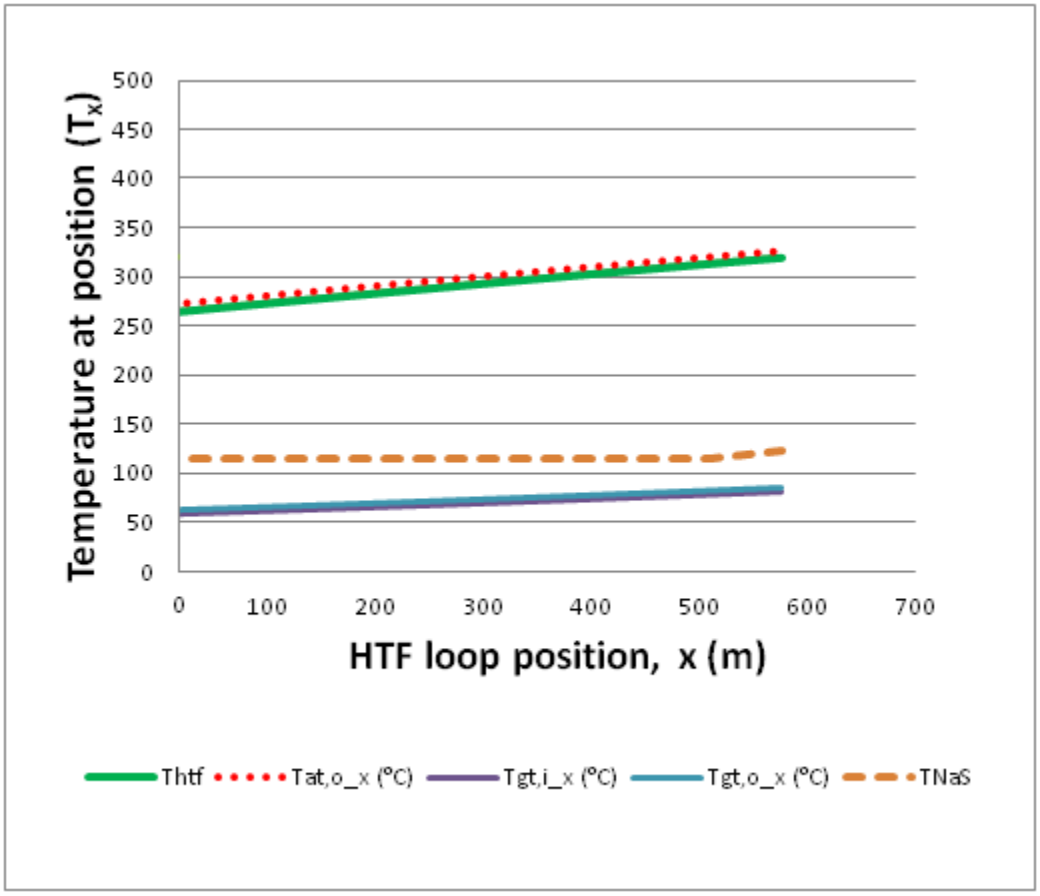

Figure 23: Temperature profiles during the "first pass" through the HTF loop

It is important to mention that heat transfer from the HTF to the NaS cells occurs only *"after one residence time through the total power plant flow circuit"* (comprising solar field loop, header, runner and the pipework of the storage/power block) and only if the solar field HTF *"return temperature"* exceeds the initial cold temperature of the NaS cell bed. Therefore, depending on the initial temperatures of the NaS cells and other sections of the flow circuit, it is possible that the NaS cells could be *"cooled"* rather than heated, on return of the HTF to the solar field.

To keep the simulation realistic in terms of timescales, before the second pass was simulated, a transient time of approximately 5 hours was calculated (based on the DNI values of the first HTF pass), for heat transfer to the thermal mass of pipework in the conceptual solar field. This time delay would allow the entire solar field (excluding thermal storage tanks and heat exchanger blocks) to be brought up to the first pass HTF operating temperature of the 130°C. These calculations are omitted here for brevity, but are presented for the reader's reference in Appendix 1.

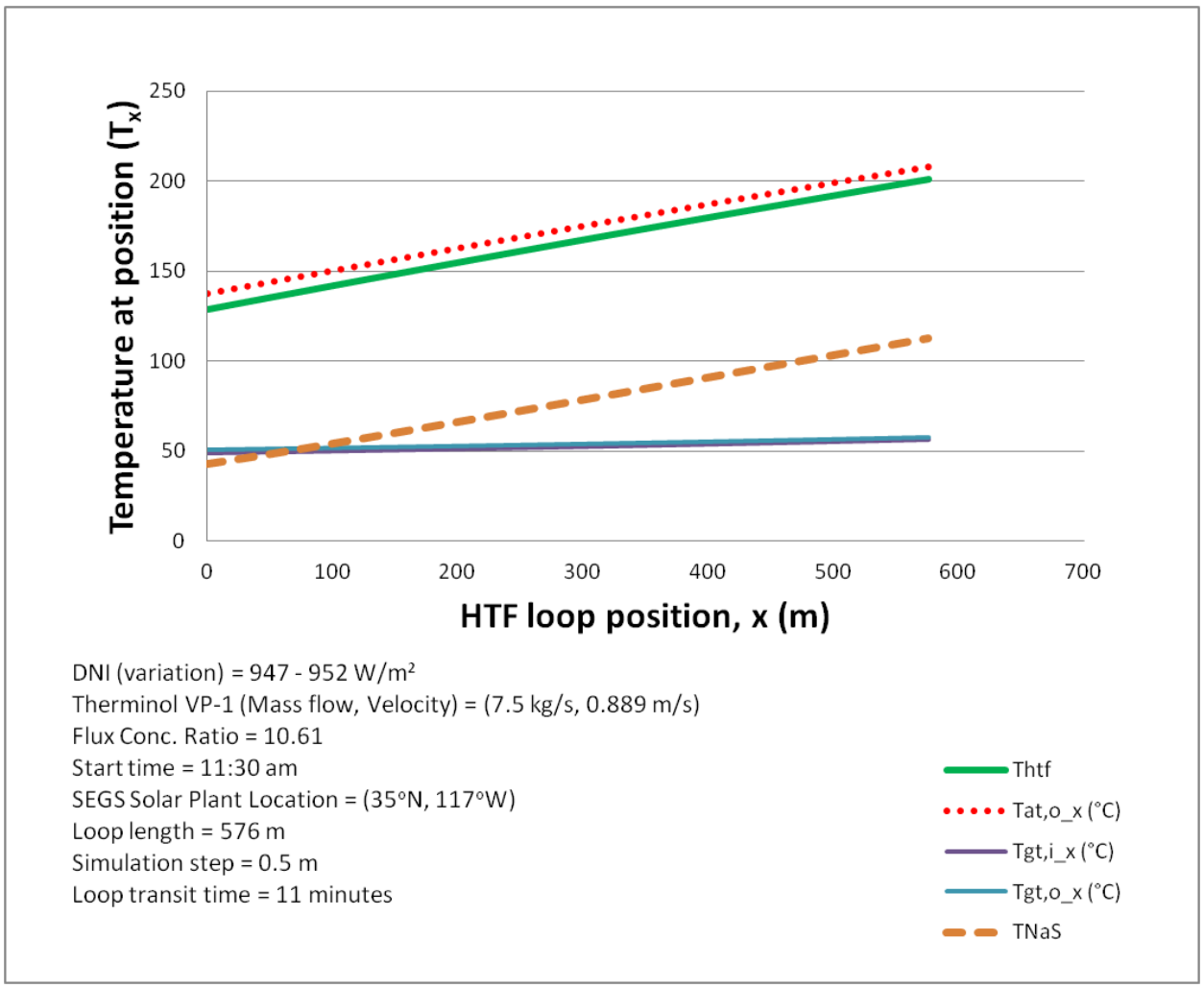

Figure 24: Second pass of Therminol VP-1 HTF through a representative loop in the solar field

In the "second pass" (Figure 24), the HTF which had been previously held at 130°C until it had brought the entire plant pipe work up to temperature, is now passed through the 576 m flow loop. As the DNI value at this time of day (11:30 am) has now approached the rated (solar noon)

value, the mass flow was increased to a rated 7.5 kg/s resulting in a shorter transit time of 11 minutes. The outlet HTF temperature was seen to rise to a new value of approximately 200^{o}C during this transit time.

At this point, it is important to point out, that this new HTF outlet temperature of 200^{o}C will not be seen again at the HTF loop inlet until the entire PTC plant pipework has been heated to this temperature. Based on the 5-hour time delay calculated for a 100K rise, it is evident that with only 12 hours of solar radiation per day, it is impossible to heat up the entire plant from a cold temperature of 20^{o}C to a power cycle temperature of approximately 400^{o}C in one day without utilizing a gas fired boiler to initially heat up the system. This must be done when commissioning new plants and these calculations served mainly to show the level of delay that would be encountered when heating up the conceptual solar field.

From this simulation point onward, it is assumed that all pipe work in the solar field had already been heated up to the power cycle operating temperature of 400^{o}C. However, the 18-minute delay between HTF loop exit and re-entry in the solar field was still observed for all ensuing simulations. Observing this delay, the *"third pass"* start time for HTF flow through the solar field (Figure 25) was calculated as follows:

3rd pass start time = 11:30am (2nd pass start time) + (11 mins in solar field transit time) + (18 mins delay for return to solar field) = 11:58 am.

Thus 11:58 am was used as the start time of the *"3rd HTF pass"* through the solar field. During this pass, and owing to the temperature gradient of the HTF flowing over the NaS battery tube in the loop, the simulation shows that now about half of the NaS cells (towards the end of the loop) would be experiencing phase change. This is shown by the constant temperature of these cells in the simulation. Although rea life phase change of the NaS cells does occur in the 115 - 120^{o}C, the first pass HTF temperature value of 130^{o}C was used for convenience as the "simulation phase change temperature" for the entire solar field. This does not adversely affect at the meaning of the results as under real conditions the only difference would be a slightly lower phase change temperature.

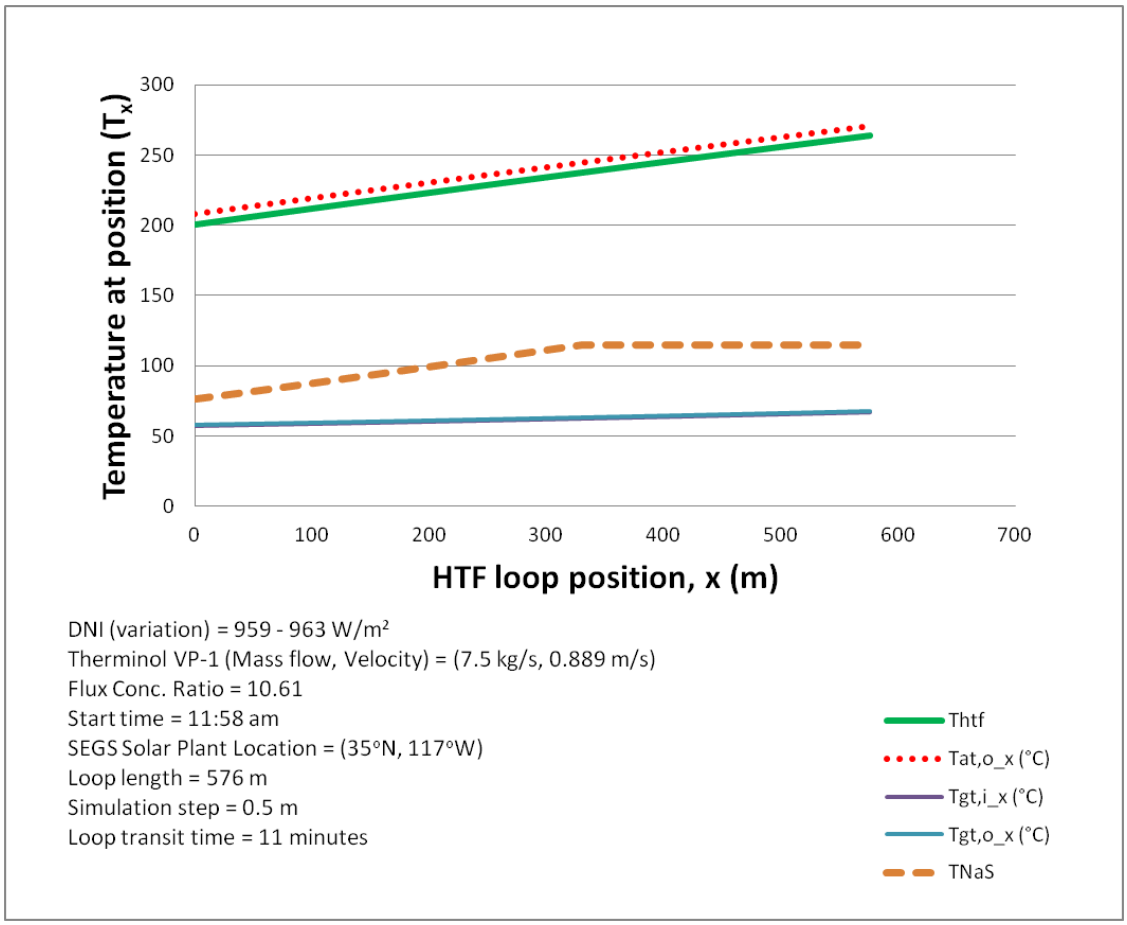

Figure 25: Third pass of Therminol VP-1 HTF through a representative loop in the solar field

At the end of the fourth pass (Figure 26), most of the NaS cells in the HTF loop would have been still been undergoing phase change, with only a few cells near the end of the loop having fully completed their phase change.

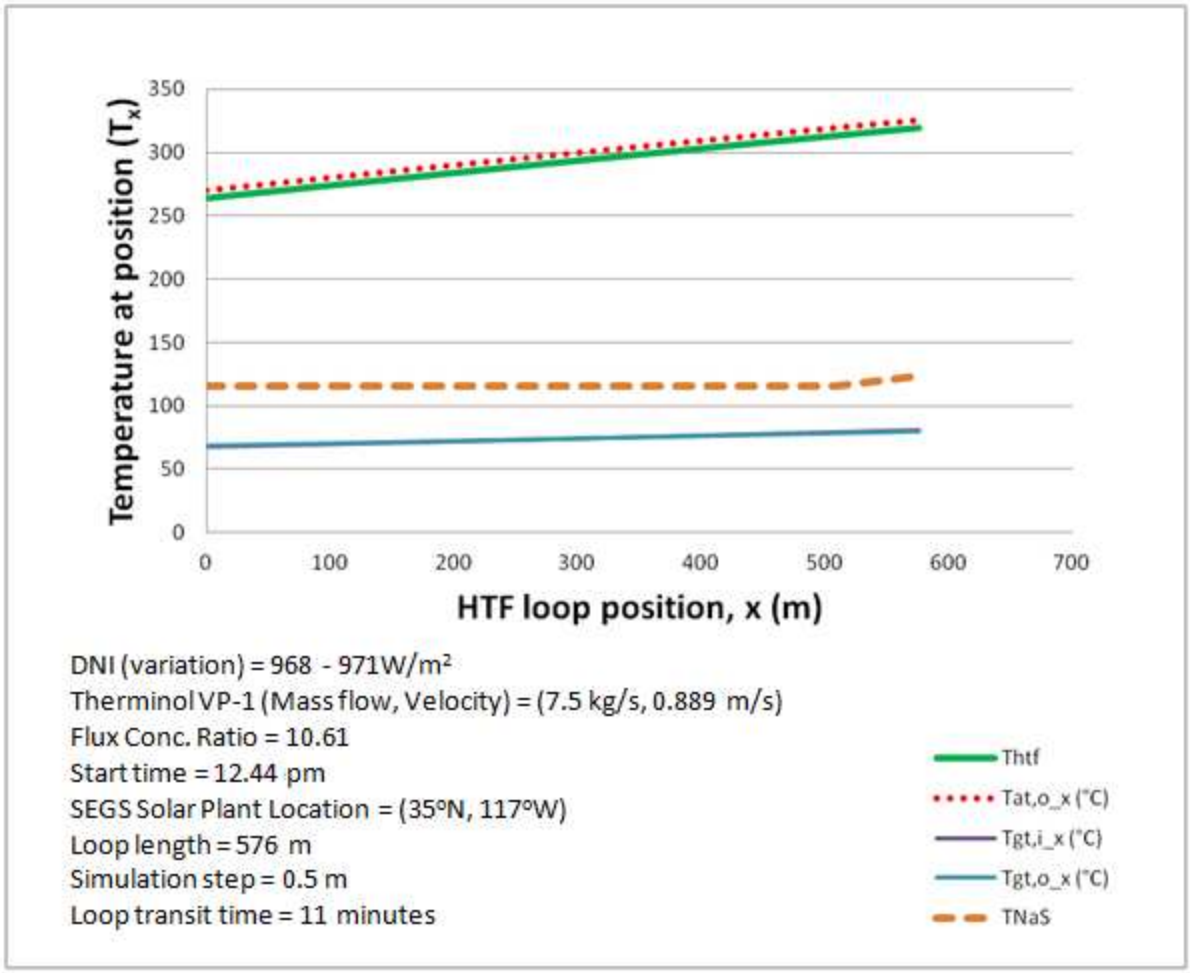

Figure 26: Fourth pass of Therminol VP-1 HTF through a representative loop in the solar field

By the time of the fifth pass (Figure 27), most of the NaS cells in the loop would have passed through phase change and would have again begun to experience a temperature rise. There is a slight fall in the gradient of the slope near the end of this profile. This was influenced by the previous gradient at the end of the fourth pass, resulting in a lower driving force for heat transfer to the NaS cells during the fifth pass.

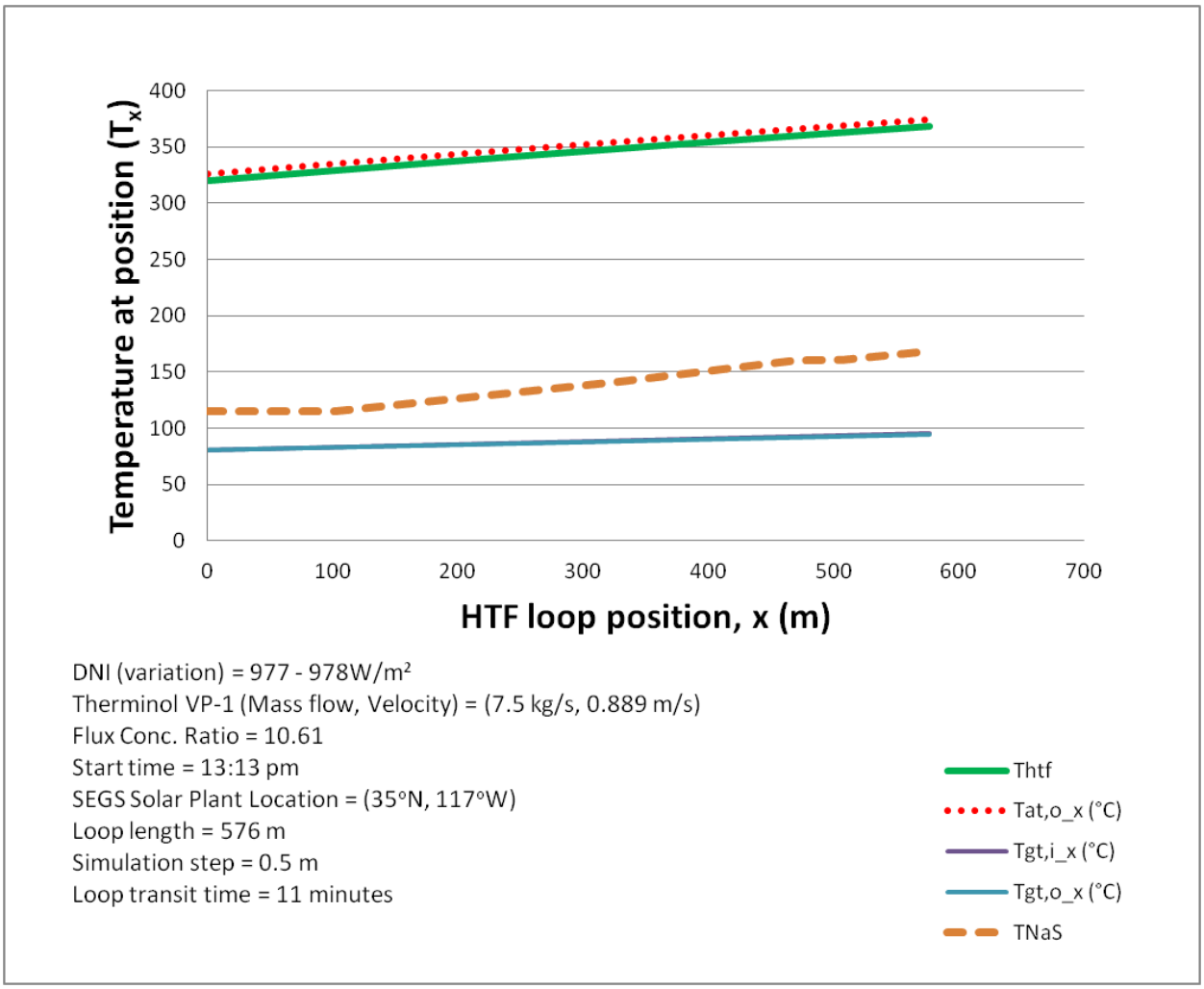

Figure 27: Fifth pass of Therminol VP-1 HTF through a representative loop in the solar field

At the time of the sixth pass (Figure 28), simulations revealed that all the NaS cells would have completed phase change, and that cell temperatures would continue to rise, approaching that of the average HTF temperature.

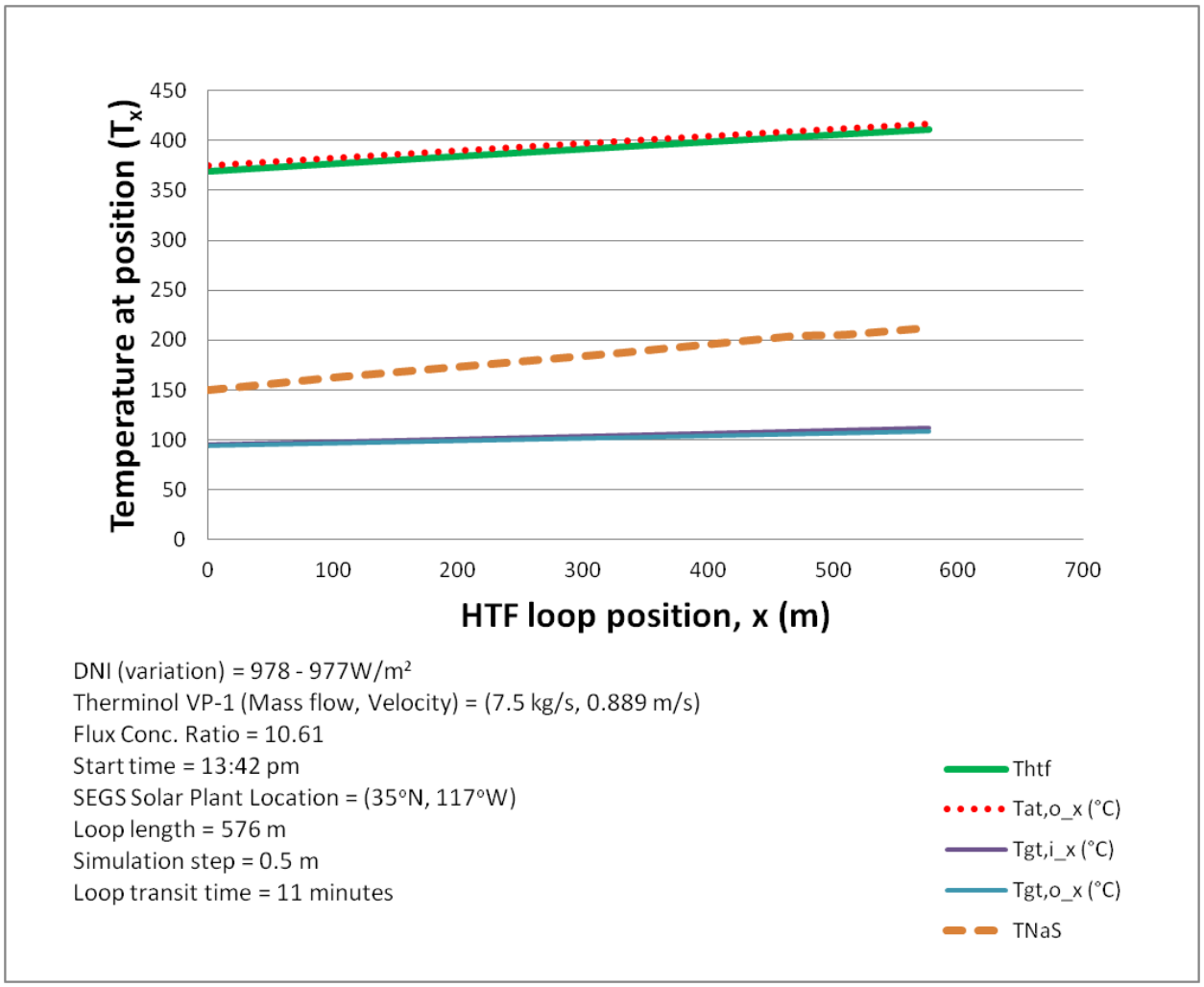

Figure 28: Sixth pass of Therminol VP-1 HTF through a representative loop in the solar field

For the 7th to 13th passes, (**Error! Reference source not found.** to **Error! Reference source not found.**) results show the NaS battery temperature gradually approaching that of the HTF. In all these passes the HTF is assumed to be *"cooled down"* by heat transfer in the plant's thermal storage system and returned to the solar field at a fairly constant temperature of 300°C, as would be the case in any traditional PTC utilizing a Therminol VP-1 heat transfer fluid. These plots are not shown for the sake of brevity in this work.

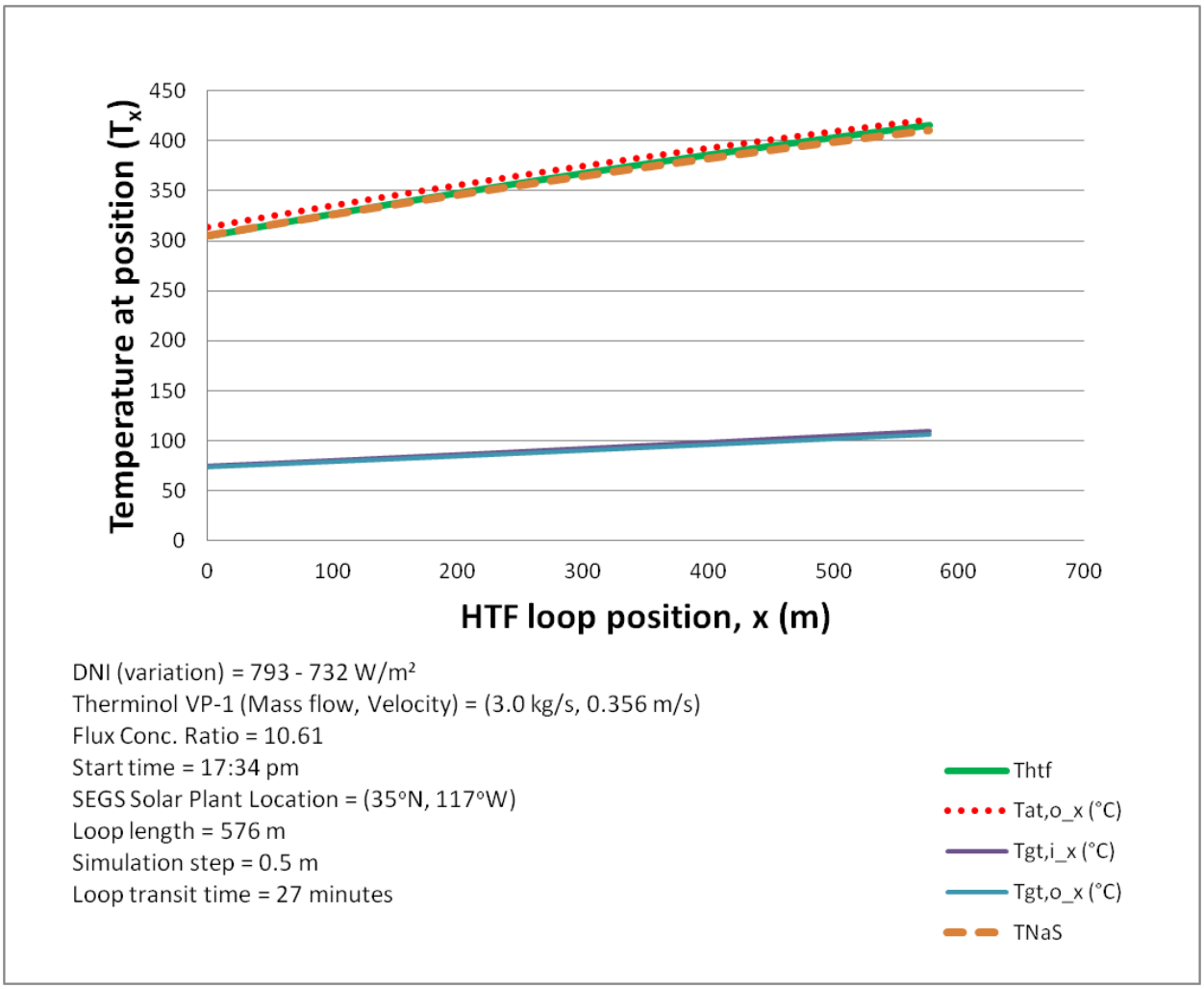

Figure 29: Fourteenth and final pass of Therminol VP-1 HTF through a loop in EES solar field

At the time of the fourteenth pass, the NaS cells would have finally reached thermal equilibrium with the HTF (Figure 29) and be ready for charging. This charge/discharge operation will be presented in a follow-up article to this work.

8. Summary and Conclusion

In this paper, both the conceptual representation and system of mathematical models describing the heat transfer processes in a novel Electrical Energy Storage (EES) PTC receiver have been presented. The EES receiver is a novel conceptual receiver with integrated electrical energy

storage, a concept that is of critical importance in the context of the Renewable Energy revolution, Smart Grid Demand Support and many other potential ancillary power support services for existing utility grids. In this paper, the conceptual EES receiver was mathematically modelled through the numerical solution of a quasi-transient system of 10 steady state and 2 transient equations, given in terms of the important nodular temperatures and heat fluxes of the EES receiver.

It was shown that the steady state equations were combined to produce a highly non-linear equation in $\dot{q}'_{cond,at}$, the heat flux conducted through the absorber wall flux, which was solved using the goalseek tool available in Microsoft Excel. The solution to this *"main"* equation served as the backbone of a Visual Basic macro coded in Microsoft Excel for the incremental solution of discretized transient equations along the axial length of the HTF flow path. To the researcher's best knowledge, this may be one of the few or probably singular published cases where a complete Solar Parabolic Trough system model has been solved in this manner and outside of the use of established software packages such as MATLAB/ Simulink, TRNSYS or Scilab/Xcos.

With regards to the initial heating up to operating temperature of the conceptual EES receiver solar field (with the NaS cells held under adiabatic conditions), both NREL test results and validated models of other researchers were used to assess model predictions. It was found that the model provides valid predictions of the key operating parameters, but over, or under predicts these parameters slightly because of the idealistic heat transfer conditions assumed *(ignoring of annular convective losses in glass cover and conductive losses from the absorber tube)*. It was also seen that the EES receiver exhibits a relatively higher heat loss, which is directly influenced by its much larger absorber surface area and consequently lower flux concentration ratio.

Despite these factors however, the results of the model have been validated, as key plant performance indicators (at working temperatures of 300-400^{o}C) such as useful energy gain (3000-4000 W/m) and collector efficiency (75 – 61%) are well within the expected operational range for standard solar PTC fields when the model was forced to run under identical operating conditions[98] . Most importantly under adiabatic NaS cell conditions, the computational results have been shown to be highly comparable to experimentally validated data[99,102,103] for standard PTC receivers currently deployed in PTC power plants around the globe.

A follow up article will present results from charge/discharge simulations of this conceptual EES receiver in a typical 50 MW (Andasol Type) PTC power plant.

References

[1] Patnode AM. Simulation and Performance Evaluation of Parabolic Trough Solar Power Plants. University of Wisconsin-Madison, 2006.

[2] Geyer M, Lüpfert E, Osuna R, Nava P, Langenkamp J, Mandelberg E. EUROTROUGH - Parabolic Trough Collector Developed for Cost Efficient Solar Power Generation. 11th SolarPACES International Symposium on Concentrated Solar Power and Chemical Energy Technologies 2002:7.

[3] Kalogirou SA. Solar thermal collectors and applications. Progress in Energy and Combustion Science 2004;30:231–95.

[4] Kalogirou S. Solar Energy Engineering: Processes and Systems. Solar Energy Engineering 2009:iv–iv. doi:10.1016/B978-0-12-374501-9.00014-5.

[5] Hernández-Moro J, Martínez-Duart JM. Analytical model for solar PV and CSP electricity costs: Present LCOE values and their future evolution. Renewable and Sustainable Energy Reviews 2013;20:119–32. doi:10.1016/j.rser.2012.11.082.

[6] Hussien ZF, Cheung LW, Siam MFM, Ismail AB. Modeling of Sodium Sulfur Battery for Power System Applications. Elektrika Journal of Electrical Engineering 2007;9:66–72.

[7] Kondoh J, Ishii I, Yamaguchi H, Murata A, Otani K, Sakuta K, et al. Electrical energy storage systems for energy networks. Energy Conversion and Management 2000;41:1863–74.

[8] Chung LW, Siam MFM, Ismail AB, Hussien ZF. Modeling and simulation of sodium sulfur battery for battery energy storage system and custom power devices. National Power and Energy Conference, PECon 2004 - Proceedings 2004:205–10.

[9] Fernández-García A, Zarza E, Valenzuela L, Pérez M. Parabolic-trough solar collectors and their applications. Renewable and Sustainable Energy Reviews 2010;14:1695–721.

[10] Sudworth JL. The sodium/sulphur battery. Journal of Power Sources 1984;11:143–54. doi:10.1016/0378-7753(84)80080-4.

[11] Wynn Jones I. Recent advances in the development of sodium-sulphur batteries for load levelling and motive power applications. Electrochimica Acta 1977;22:681–8.

[12] Tao YB, He YL. Numerical study on coupled fluid flow and heat transfer process in parabolic trough solar collector tube. Solar Energy 2010;84:1863–72.

[13] Koskinen O, Breyer C. Energy Storage in Global and Transcontinental Energy Scenarios: A Critical Review. Energy Procedia 2016;99:53–63. doi:10.1016/j.egypro.2016.10.097.

[14] Landry M, Gagnon Y. Energy Storage: Technology Applications and Policy Options. Energy Procedia 2015;79:315–20. doi:10.1016/j.egypro.2015.11.494.

[15] Gallo AB, Simões-Moreira JR, Costa HKM, Santos MM, Moutinho dos Santos E. Energy storage in the energy transition context: A technology review. Renewable and Sustainable Energy Reviews 2016;65:800–22. doi:10.1016/j.rser.2016.07.028.

[16] Lombardi P, Schwabe F. Sharing economy as a new business model for energy storage systems. Applied Energy 2017;188:485–96. doi:10.1016/j.apenergy.2016.12.016.

[17] Lefebvre D, Tezel FH. A review of energy storage technologies with a focus on adsorption thermal energy storage processes for heating applications. Renewable and Sustainable Energy Reviews 2017;67:116–25. doi:10.1016/j.rser.2016.08.019.

[18] Ould Amrouche S, Rekioua D, Rekioua T, Bacha S. Overview of energy storage in renewable energy systems. International Journal of Hydrogen Energy 2016;41:20914–27. doi:10.1016/j.ijhydene.2016.06.243.

[19] Mahlia TMI, Saktisahdan TJ, Jannifar A, Hasan MH, Matseelar HSC. A review of available methods and development on energy storage; technology update. Renewable and Sustainable Energy Reviews 2014;33:532–45. doi:10.1016/j.rser.2014.01.068.

[20] Yekini Suberu M, Wazir Mustafa M, Bashir N. Energy storage systems for renewable energy power sector integration and mitigation of intermittency. Renewable and Sustainable Energy Reviews 2014;35:499–514. doi:10.1016/j.rser.2014.04.009.

[21] Castillo A, Gayme DF. Grid-scale energy storage applications in renewable energy integration: A survey. Energy Conversion and Management 2014;87:885–94. doi:10.1016/j.enconman.2014.07.063.

[22] Akinyele DO, Rayudu RK. Review of energy storage technologies for sustainable power networks. Sustainable Energy Technologies and Assessments 2014;8:74–91. doi:10.1016/j.seta.2014.07.004.

[23] Roskilly AP, Taylor PC, Yan J. Energy storage systems for a low carbon future – in need of an integrated approach. Applied Energy 2015;137:463–6. doi:10.1016/j.apenergy.2014.11.025.

[24] Aneke M, Wang M. Energy storage technologies and real life applications – A state of the art review. Applied Energy 2016;179:350–77. doi:10.1016/j.apenergy.2016.06.097.

[25] Palizban O, Kauhaniemi K. Energy storage systems in modern grids—Matrix of technologies and applications. Journal of Energy Storage 2016;6:248–59. doi:10.1016/j.est.2016.02.001.

[26] Kousksou T, Bruel P, Jamil A, El Rhafiki T, Zeraouli Y. Energy storage: Applications and challenges. Solar Energy Materials and Solar Cells 2014;120:59–80. doi:10.1016/j.solmat.2013.08.015.

[27] Bocklisch T. Hybrid energy storage approach for renewable energy applications. Journal of Energy Storage 2016;8:311–9. doi:10.1016/j.est.2016.01.004.

[28] Chong LW, Wong YW, Rajkumar RK, Rajkumar RK, Isa D. Hybrid energy storage systems and control strategies for stand-alone renewable energy power systems. Renewable and Sustainable Energy Reviews 2016;66:174–89. doi:10.1016/j.rser.2016.07.059.

[29] Hemmati R, Saboori H. Emergence of hybrid energy storage systems in renewable energy and transport applications – A review. Renewable and Sustainable Energy Reviews 2016;65:11–23. doi:10.1016/j.rser.2016.06.029.

[30] Zimmermann T, Keil P, Hofmann M, Horsche MF, Pichlmaier S, Jossen A. Review of system topologies for hybrid electrical energy storage systems. Journal of Energy Storage 2016;8:78–90. doi:10.1016/j.est.2016.09.006.

[31] Arani AAK, Karami H, Gharehpetian GB, Hejazi MSA. Review of Flywheel Energy Storage Systems structures and applications in power systems and microgrids. Renewable and Sustainable Energy Reviews 2017;69:9–18. doi:10.1016/j.rser.2016.11.166.

[32] Mousavi G SM, Faraji F, Majazi A, Al-Haddad K. A comprehensive review of Flywheel Energy Storage System technology. Renewable and Sustainable Energy Reviews 2017;67:477–90. doi:10.1016/j.rser.2016.09.060.

[33] Pena-Alzola R, Sebastián R, Quesada J, Colmenar A. Review of Flywheel based Energy Storage Systems. International Conference on Power Engineering, Energy and Electrical Drives 2011. doi:10.1109/PowerEng.2011.6036455.

[34] Buckles W, Ilassenzahl W V. Superconducting Magnetic Energy Storage. IEEE Power Engineering Review 2000. doi:10.1109/39.841345.

[35] Raman SR, Xue XD, Cheng KWE. Review of charge equalization schemes for Li-ion battery and super-capacitor energy storage systems. 2014 International Conference on Advances in Electronics, Computers and Communications, ICAECC 2014, 2015. doi:10.1109/ICAECC.2014.7002471.

[36] Soori PK, Shetty SC, Chacko S. Application of super capacitor energy storage in microgrid system. 2011 IEEE GCC Conference and Exhibition, GCC 2011, 2011. doi:10.1109/IEEEGCC.2011.5752605.

[37] Rossi F, Castellani B, Nicolini A. Benefits and Challenges of Mechanical Spring Systems for Energy Storage Applications. Energy Procedia 2015;82:805–10. doi:10.1016/j.egypro.2015.11.816.

[38] de Oliveira e Silva G, Hendrick P. Pumped hydro energy storage in buildings. Applied Energy 2016;179:1242–50. doi:10.1016/j.apenergy.2016.07.046.

[39] Rehman S, Al-Hadhrami LM, Alam MM. Pumped hydro energy storage system: A technological review. Renewable and Sustainable Energy Reviews 2015. doi:10.1016/j.rser.2014.12.040.

[40] Budt M, Wolf D, Span R, Yan J. Compressed Air Energy Storage – An Option for Medium

to Large Scale Electrical-energy Storage. Energy Procedia 2016;88:698–702. doi:10.1016/j.egypro.2016.06.046.

[41] Alotto P, Guarnieri M, Moro F. Redox flow batteries for the storage of renewable energy: A review. Renew Sust Energy Rev 2014. doi:10.1016/j.rser.2013.08.001.

[42] Weber A, Mench M, Meyers J, Ross P, Gostick J, Liu Q. Redox flow batteries: a review. Journal of Applied Electrochemistry 2011.

[43] Viswanathan V, Crawford A, Stephenson D, Kim S, Wang W, Li B, et al. Cost and performance model for redox flow batteries. J Power Sources 2014. doi:10.1016/j.jpowsour.2012.12.023.

[44] Skyllas-Kazacos M, Tomazic G. Redox Flow Batteries. 2014. doi:10.1016/B978-0-444-62616-5.00017-6.

[45] Staffell I, Rustomji M. Maximising the value of electricity storage. Journal of Energy Storage 2016;8:212–25. doi:10.1016/j.est.2016.08.010.

[46] Banham-Hall DD, Taylor GA, Smith CA, Irving MR. Frequency control using Vanadium redox flow batteries on wind farms. IEEE Power and Energy Society General Meeting, 2011. doi:10.1109/PES.2011.6039520.

[47] Tewari S. Potential of Sodium-Sulfur Battery Energy Storage to Enable Further Integration of Wind. Energy Storage for Smart Grids, Elsevier; 2015, p. 67–95. doi:10.1016/B978-0-12-410491-4.00003-8.

[48] Andriollo M, Benato R, Dambone Sessa S, Di Pietro N, Hirai N, Nakanishi Y, et al. Energy intensive electrochemical storage in Italy: 34.8MW sodium–sulphur secondary cells. Journal of Energy Storage 2016;5:146–55. doi:10.1016/j.est.2015.12.003.

[49] Obara S, Morizane Y, Morel J. Economic efficiency of a renewable energy independent microgrid with energy storage by a sodium–sulfur battery or organic chemical hydride. International Journal of Hydrogen Energy 2013;38:8888–902. doi:10.1016/j.ijhydene.2013.05.036.

[50] Rodrigues EMG, Osório GJ, Godina R, Bizuayehu AW, Lujano-Rojas JM, Matias JCO, et al. Modelling and sizing of NaS (sodium sulfur) battery energy storage system for extending wind power performance in Crete Island. Energy 2015;90:1606–17. doi:10.1016/j.energy.2015.06.116.

[51] Suárez C, Iranzo A, Pino FJ, Guerra J. Transient analysis of the cooling process of molten salt thermal storage tanks due to standby heat loss. Applied Energy 2015. doi:10.1016/j.apenergy.2014.12.082.

[52] Herrmann U, Kelly B, Price H. Two-tank molten salt storage for parabolic trough solar power plants. Energy 2004. doi:10.1016/S0360-5442(03)00193-2.

[53] Herrmann U, Kearney DW. Survey of Thermal Energy Storage for Parabolic Trough Power Plants. Journal of Solar Energy Engineering 2002. doi:10.1115/1.1467601.

[54] Flueckiger SM, Yang Z, Garimella S V. Review of Molten-Salt Thermocline Tank Modeling for Solar Thermal Energy Storage. Heat Transfer Engineering 2013. doi:10.1080/01457632.2012.746152.

[55] Pacheco JE, Showalter SK, Kolb WJ. Development of a Molten-Salt Thermocline Thermal Storage System for Parabolic Trough Plants. Journal of Solar Energy Engineering 2002;124:153–9.

[56] Brosseau D, Kelton JW, Ray D, Edgar M, Chisman K, Emms B. Testing of Thermocline Filler Materials and Molten-Salt Heat Transfer Fluids for Thermal Energy Storage Systems in Parabolic Trough Power Plants. Journal of Solar Energy Engineering 2005;127:109.

[57] Flueckiger S, Yang Z, Garimella S V. An integrated thermal and mechanical investigation of molten-salt thermocline energy storage. Applied Energy 2011;88:2098–105.

[58] Zhang M, Xu C, Du X, Amjad M, Wen D. Off-design performance of concentrated solar heat and coal double-source boiler power generation with thermocline energy storage. Applied Energy 2017;189:697–710. doi:10.1016/j.apenergy.2016.12.095.

[59] Biencinto M, Bay??n R, Rojas E, Gonz??lez L. Simulation and assessment of operation strategies for solar thermal power plants with a thermocline storage tank. Solar Energy 2014;103:456–72.

[60] Yin H, Ding J, Jiang R, Yang X. Thermocline characteristics of molten-salt thermal energy storage in porous packed-bed tank. Applied Thermal Engineering 2017. doi:10.1016/j.applthermaleng.2016.08.214.

[61] Xu C, Wang Z, He Y, Li X, Bai F. Parametric study and standby behavior of a packed-bed molten salt thermocline thermal storage system. Renewable Energy 2012. doi:10.1016/j.renene.2012.04.017.

[62] Yang Z, Garimella S V. Thermal analysis of solar thermal energy storage in a molten-salt thermocline. Solar Energy 2010. doi:10.1016/j.solener.2010.03.007.

[63] Li P, Van Lew J, Karaki W, Chan C, Stephens J, Wang Q. Generalized charts of energy storage effectiveness for thermocline heat storage tank design and calibration. Solar Energy 2011. doi:10.1016/j.solener.2011.05.022.

[64] Kolb GJ. Evaluation of Annual Performance of 2-Tank and Thermocline Thermal Storage Systems for Trough Plants. Journal of Solar Energy Engineering 2011. doi:10.1115/1.4004239.

[65] Wegeng RS, TeGrotenhuis WE, Mankins JC. Solar thermochemical production of fuels. Collection of Technical Papers - 5th International Energy Conversion Engineering Conference 2007. doi:doi:10.2514/6.2007-4709.

[66] Tamme R, Buck R, Epstein M, Fisher U, Sugarmen C. Solar Upgrading of Fuels for Generation of Electricity. Journal of Solar Energy Engineering 2001. doi:10.1115/1.1353177.

[67] Conibeer GJ, Richards BS. A comparison of PV/electrolyser and photoelectrolytic technologies for use in solar to hydrogen energy storage systems. International Journal of Hydrogen Energy 2007. doi:10.1016/j.ijhydene.2006.09.012.

[68] Wang Z, Roberts RR, Naterer GF, Gabriel KS. Comparison of thermochemical, electrolytic, photoelectrolytic and photochemical solar-to-hydrogen production technologies. International Journal of Hydrogen Energy, 2012. doi:10.1016/j.ijhydene.2012.03.057.

[69] Chen J, Yang D, Song D, Jiang J, Ma A, Hu MZ, et al. Recent progress in enhancing solar-to-hydrogen efficiency. Journal of Power Sources 2015. doi:10.1016/j.jpowsour.2015.01.073.

[70] Bilgen E, Galindo J. High temperature solar reactors for hydrogen production. International Journal of Hydrogen Energy 1981. doi:10.1016/0360-3199(81)90002-1.

[71] Vishnevetsky I, Epstein M. Production of hydrogen from solar zinc in steam atmosphere. International Journal of Hydrogen Energy 2007. doi:10.1016/j.ijhydene.2007.04.004.

[72] Lovegrove K, Luzzi A, McCANN M, Freitag O. Exergy Analysis of Ammonia-Based Solar Thermochemical Power Systems. Solar Energy 1999. doi:10.1016/S0038-092X(98)00132-7.

[73] Li TX, Wu S, Yan T, Xu JX, Wang RZ. A novel solid–gas thermochemical multilevel sorption thermal battery for cascaded solar thermal energy storage. Applied Energy 2016;161:1–10. doi:10.1016/j.apenergy.2015.09.084.

[74] Li TX, Wang RZ, Yan T, Ishugah TF. Integrated energy storage and energy upgrade, combined cooling and heating supply, and waste heat recovery with solid-gas thermochemical sorption heat transformer. International Journal of Heat and Mass Transfer 2014. doi:10.1016/j.ijheatmasstransfer.2014.04.046.

[75] Abedin AH. Thermochemical Energy Storage Systems : Modelling , Analysis and Design. Elsevier Inc.; 2010. doi:10.1016/B978-0-12-803440-8/00017-8.

[76] Kerskes H. Thermochemical Energy Storage. Storing Energy: With Special Reference to Renewable Energy Sources, Elsevier Inc.; 2016, p. 345–72.

[77] Gur I, Sawyer K, Prasher R. Searching for a Better Thermal Battery. Science 2012. doi:10.1126/science.1218761.

[78] Yu M, McCulloch WD, Huang Z, Trang BB, Lu J, Amine K, et al. Solar-powered electrochemical energy storage: an alternative to solar fuels. J Mater Chem A 2016;0:1–17.

[79] Masset P, Guidotti RA. Thermal activated (thermal) battery technology. Part II. Molten salt electrolytes. Journal of Power Sources 2007. doi:10.1016/j.jpowsour.2006.10.080.

[80] Guidotti RA, Masset PJ. Thermally activated ("thermal") battery technology. Part IV. Anode materials. Journal of Power Sources 2008. doi:10.1016/j.jpowsour.2008.04.090.

[81] Abedin A, Rosen M. A Critical Review of Thermochemical Energy Storage Systems. Open Renewable Energy Journal 2011;4:42–6. doi:10.2174/1876387101004010042.

[82] Nation DD, Heggs PJ, Dixon-Hardy DW. A conceptual Photo-Electro-Chemical-Thermal (PECT) receiver for a net zero CO2 emissions SPTC plant. 30th ISES Biennial Solar World Congress 2011, SWC 2011, vol. 5, 2011.

[83] Sohr O, Möllenhoff M, Kuckelkorn T. Laser induced release of encapsulated noble gas in SCHOTT receiver. Energy Procedia, vol. 49, Elsevier Ltd; 2013, p. 524–9.

[84] Kalogirou SA. A detailed thermal model of a parabolic trough collector receiver. Energy 2012;48:298–306.

[85] Padilla RV, Demirkaya G, Goswami DY, Stefanakos E, Rahman MM. Heat transfer analysis of parabolic trough solar receiver. Applied Energy 2011;88:5097–110.

[86] Anggono J. Mullite Ceramics: Its Properties, Structure, and Synthesis. Jurnal Teknik Mesin 2005;7:1–10.

[87] Pierson HO. Characteristics and Properties of Silicon Carbide and Boron Carbide. Handbook of Refractory Carbides and Nitrides Properties, Characteristics, Processing and Applications 1996:137–55. doi:10.1016/B978-081551392-6.50009-X.

[88] Kearney D, Kelly B, Herrmann U, Cable R, Pacheco J, Mahoney R, et al. Engineering aspects of a molten salt heat transfer fluid in a trough solar field. Energy 2004;29:861–70.

[89] Quaschning V. Solar Thermal Power Plants: Technolgy Fundamentals. Renewable Energy World 2003:109–13. http://www.volker-quaschning.de/articles/fundamentals2/index_e.php (accessed October 31, 2016).

[90] Rolim MM, Fraidenraich N, Tiba C. Analytic modeling of a solar power plant with parabolic linear collectors. Solar Energy 2009;83:126–33.

[91] Wesoff E. SunPower Holds World Record for Most Efficient Rooftop Solar Panel, Again. PV Manufacturing Market Update 2016. https://www.greentechmedia.com/articles/read/SunPower-Again-Holds-Record-For-Worlds-Most-Efficient-Rooftop-Solar-Panel (accessed October 31, 2016).

[92] SM. Solar Thermal Power Plants. Bine Information Service 2016. http://www.bine.info/en/publications/publikation/solarthermische-kraftwerke-werden-praxis/solarthermische-kraftwerke-1/ (accessed October 31, 2016).

[93] Price H, Lüpfert E, Kearney D, Zarza E, Cohen G, Gee R, et al. Advances in Parabolic Trough Solar Power Technology. Journal of Solar Energy Engineering 2002;124:109. doi:10.1115/1.1467922.

[94] Duffie JA, Beckman WA. Solar Engineering of Thermal Processes: Fourth Edition. John Wiley and Sons; 2013.

[95] H. Tokoi, N. Watahiki, S. Izumi, K. Satoh. Evaluation of Sodium Sulfur Cell Characteristics using an in Situ X-ray computed Tomogram. Journal of the Electrochemical Society 1999;146:4005–8.

[96] Jeffreson CP. Prediction of breakthrough curves in packed beds. AIChE Journal 1972;18:409–20.

[97] Gibbard HF. Thermal Properties of Battery Systems. Journal of The Electrochemical Society 1978;125:353.

[98] Russell F. Heat Transfer Analysis and Modeling of a Parabolic Trough Solar Receiver Implemented in Engineering Equation Solver. National Renewable Energy Laboratory 2003:164. doi:NREL/TP-550-34169.

[99] Dudley VE, Kolb GJ, Mahoney AR, Mancini TR, Matthews CW, Sloan M, et al. Test results: SEGS LS-2 solar collector. Sandia National Laboratories 1994.

[100] Klein S, Alvarado F. Engineering equation solver. F-Chart Software, Box 2002:1–2.

[101] Forristall R. Heat Transfer Analysis and Modeling of a Parabolic Trough Solar Receiver Implemented in Engineering Equation Solver. 2003.

[102] Burkholder F, Kutscher CF. Heat loss testing of Schott's 2008 PTR70 parabolic trough receiver. NREL Technical Report 2009:58.

[103] Burkholder F, Kutscher C. Heat-Loss Testing of Solel's UVAC3 Parabolic Trough Receiver. NREL Technical Report 2008;TP-550-423:19.

[104] Solutia. Therminol VP-1 Properties Datasheet n.d. http://twt.mpei.ac.ru/tthb/hedh/htf-vp1.pdf.

[105] Jones SA, Pitz-Paal, P.S., Blair, N., Cable R. TRNSYS Modelling of the SEGS VI Parabolic Trough Solar Electric Generating System. Proceeddings of Solar Forum 2001, 2001; Washington DC, 2001.

[106] Khaled A. Technical and Economic Performance of Parabolic Trough in Jordan. Universitat Kassel, 2012.

[107] Wagner MJ, Gilman P. Technical Manual for the Physical Trough model. System Advisor Model Documentation. 2011.

[108] Kelly B, Kearney D. Parbolic Trough Solar System Piping Model. 2006.

Appendix 1

Time Delay Calculations for Heating Thermal Mass of an Andasol-1 Type Solar Field

It was important to develop a rough estimate of the maximum time delay between HTF exit and re-entry, in a representative HTF loop. A schematic depicting the layout typical of the Andasol-1 power plant layout (Figure 30) was therefore used to estimate the HTF flow distance between the power block and one of the HTF loops furthest from it (loop 117). Based on a *"rough"* calculation, the average distance the HTF travels to and from this loop, is approximately 2000 m.

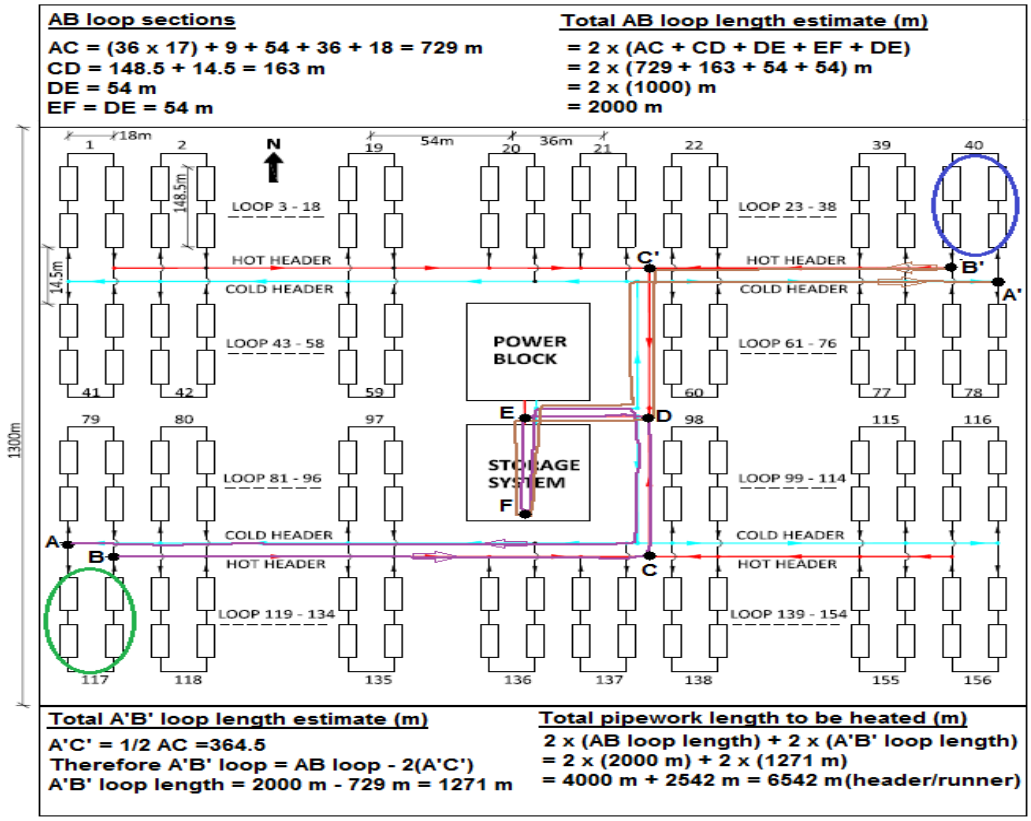

Figure 30: Schematic illustrating the layout of an Andasol-1 type PTC solar field (Adapted:[106]**)**

Further, for estimation of the time delay associated with HTF's exit and re-entry into the solar field, it is also necessary to know the average HTF velocity through this *"estimated 2000 m of pipework"*. In the System Advisor Model (SAM) '*Technical Manual for the Physical Trough Model'* [107], Wagner and Gilman of NREL, USA refer to PTC plants as having three different pumps for the HTF flow loop. These pumps are used to connect the three main piping sections of the plant, (power block, solar field and header/runners). Therefore, as different flows are typical across the three main sections of HTF flow circuitry, it was

inappropriate to apply the same flow velocity of 0.2964 m/s used previously for the *"first pass"* through the solar field, to the rest of pipework in the system.

According to Wagner and Gilman, the design-point HTF velocity used for PTC plants in SAM software is 1.85 m/s. Using this velocity as a *"rough estimate"*, the maximum expected time delay between solar field HTF exit and re-entry into the chosen representative loop was evaluated as follows:

$$Time\ delay\ = \frac{Total\ distance}{design\ point\ velocity}\ = \frac{2000\ m}{1.85\ m/s} = 1081\ s\ \approx\ 18\ mins$$

In the first pass, simulations revealed an HTF loop exit temperature of approximately 130°C. As stated earlier in this chapter, the EES receiver operates in conjunction standard thermal storage, but before the storage system can be charged, the *"entire 2000 m length of pipe work"* must be heated up by the *"entire solar field"*.

This requires determination of the mc_p value of the pipe work. For a worst-case scenario, the physical properties and dimensions of the largest pipe work section (runners) in a standard PTC plant were used to estimate the mc_p value of the entire 2000 m length of pipe work. Wagner and Gilman give the largest pipe size used in the SAM model as 72" schedule D steel pipe with an internal diameter of 1.778 m and a wall thickness of 34.5 mm [107].

The volume of a 2000 m length of this pipe is calculated as follows:

$$volume =\ \pi(D_o -\ D_i)^2 \times L_{pipe} = \pi(1.847\ m -\ 1.778\ m)^2 \times 6542\ m = 97.84\ m^3$$

Based on the work of Kelly and Kearney [108], the pipe work is here assumed to be ASTM A106, Grade B, seamless carbon steel pipe. The density of this carbon steel is given by industry datasheets as 7870 kg/m^3.

Therefore, the mass of pipework to be heated is given as:

$$Mass\ =\ Density \times Volume =\ 7870\ \mathrm{kg/m^3} \times 97.84\ m^3 = 7.7 \times 10^5\ \mathrm{kg} = 770\ \mathrm{tonnes}$$

The mass of absorber pipework in the entire solar field must also be heated up, before heat transfer can begin to the HTF or NaS cells. Using the *"real"* HTF loop length of 600 m, the total length of the 156 loops in the solar field is calculated as: $600\ m \times 156\ = 93{,}600\ m$

The solar field absorber pipe volume can therefore be calculated as follows:

$$volume =\ \pi(D_o -\ D_i)^2 \times L_{pipe} = \pi(0.168\ m -\ 0.154\ m)^2 \times 93600\ m\ = 57\ m^3$$

Using the same density value as for ASTM A106, Grade B, seamless carbon steel pipe, the mass of absorber pipe to be heated is given as:

$$Mass\ =\ Density \times Volume =\ 7870\ \mathrm{kg/m^3} \times 57.634\ m^3 = 454 \times 10^3\ \mathrm{kg} = 454\ \mathrm{tonnes}$$

Therefore, the total mass of power plant pipe work to be heated is given as:

$$Mass\ total\ = Mass\ (solar\ field\ pipe\ work\ +\ pipework\ connecting\ to\ power\ block)\ [\text{tonnes}]$$

$$Mass\ total = 454\ + 770 = 1224\ \text{tonnes}$$

Now, the energy captured by the HTF as it moves through each flow loop of the solar field can be calculated as:

$$Energy\ captured\ (J) = \dot{M}_{HTF}\ [\text{kg/s}] \times C_{p,HTF}[\text{J/kgK}] \times \Delta T(\text{K}) \times t\ [\text{s}]$$

The C_p value for Therminol VP-1 increases with temperature. To remain conservative, the *"cold temperature"* C_p value of 1548 J/kg.K at the 20°C start-up temperature was used in calculation. The ΔT for this calculation is 110 K ([130 – 20] °C), but a value of 100°C was used for calculation purposes. From the model simulation, the time required for one pass of the HTF through the 576 m loop at a mass flow of 2.5 kg/s (flow velocity of 0.2964 m/s) is 32 minutes. Consequently, the energy captured by the HTF flow through the single representative loop is:

$$Energy\ captured\ = 2.5\ \text{kg/s} \times 1548\ \text{J/kg.K} \times 100\text{K} \times (32 \times 60)\text{s} = 743\ \text{MJ}$$

An Andasol-1 type solar field consists of 156 loops. Assuming the same mass flow in all 156 loops the total energy capture of the entire solar field during this time can be estimated to be:

$$Solar\ field\ energy\ capture\ = (743.04 \times 156)\text{MJ} = 116\ \text{GJ}$$

It was already estimated that it would take approximately 18 minutes for the HTF to pass through the 2000 m of header/runner pipe work in the AB flow path (Figure 30) and this time is used as representative of all field loops for simulation purposes. It can be therefore concluded that on average every 18 minutes, the 2000 m length of pipe work would receive 115.914 GJ of energy from the entire solar field. This translates to a rate heat transfer rate of:

$$Heat\ transfer\ rate\ = \frac{115.914\ GJ}{(18 \times 32 \times 60)s} = 3.354\ \text{MJ/s}$$

The *"Engineering Toolbox"* website gives the specific heat of carbon steel as $0.49\ \text{kJ/kg.K}$. Therefore, the energy required to heat up the entire 1224 tonnes of pipe work also by 100 K is calculated as:

$$Required\ Pipe\ work\ Heat\ Energy\ (J) = m_{pipe\ work} \times C_{p,c-steel} \times \Delta T$$

$$Required\ Pipe\ work\ Heat\ Energy\ (\text{J}) = 1224000\ \text{kg} \times 490\ \text{J/kg.K} \times 100\text{K} = 59.95\ \text{GJ}$$

If the heat transfer rate to the pipe work is $107.33\ \text{MJ/s}$ as calculated earlier, then the total time required to reach an equilibrium temperature of 130°C is given as:

$$Heating\ time\ (s) = \frac{Required\ Pipe\ work\ Heat\ Energy\ (\text{J})}{Heat\ transfer\ rate\ (\text{J/s})}$$

$$Heating\ time\ (s) = \frac{59.95\ \text{GJ}}{3.354\ \text{MJ/s}} = 17875\ s = 4.97\ \text{h}$$

This translates to a time of approximately 5 hours, a value which may prove conservative as during this time, the actual solar (DNI value W/m^2) would have been increased beyond the maximum value of the range used in the initial 32-minute simulation.

However, this time delay does provide a useful point in time from which to continue with the initial heating-up of the solar field from beyond the 130^{o}C value. Since simulation began at 6:30 am, adding 5 hours to this time would allow simulation to continue from the 130^{o}C temperature value with a new start time of approximately 11:30 am and with HTF and NaS temperature profiles as depicted by the *"first pass"* (Figure 23).

END OF APPENDIX 1